Mon. Not. R. Astron. Soc. **376,** 609–624 (2007) doi:10.1111/j.1365-2966.2007.11451.x

Burial of the polar magnetic field of an accreting neutron star – II. Hydromagnetic stability of axisymmetric equilibria

D. J. B. Payne★ and A. Melatos
School of Physics, University of Melbourne, Parkville, VIC 3010, Australia

Accepted 2006 December 26. Received 2006 December 15; in original form 2006 September 29

ABSTRACT

The theory of polar magnetic burial in accreting neutron stars predicts that a mountain of accreted material accumulates at the magnetic poles of the star, and that, as the mountain spreads equatorward, it is confined by, and compresses, the equatorial magnetic field. Here, we extend previous, axisymmetric, Grad–Shafranov calculations of the hydromagnetic structure of a magnetic mountain up to accreted masses as high as $M_{\rm a} = 6 \times 10^{-4}\,{\rm M}_{\odot}$, by importing the output from previous calculations (which were limited by numerical problems and the formation of closed bubbles to $M_{\rm a} < 10^{-4}\,{\rm M}_{\odot}$) into the time-dependent, ideal-magnetohydrodynamic code ZEUS-3D and loading additional mass on to the star dynamically. The rise of buoyant magnetic bubbles through the accreted layer is observed in these experiments. We also investigate the stability of the resulting hydromagnetic equilibria by perturbing them in ZEUS-3D. Surprisingly, it is observed that the equilibria are marginally stable for all $M_{\rm a} \leqslant 6 \times 10^{-4}\,{\rm M}_{\odot}$; the mountain oscillates persistently when perturbed, in a combination of Alfvén and acoustic modes, without appreciable damping or growth, and is therefore not disrupted (apart from a transient Parker instability initially, which expels <1 per cent of the mass and magnetic flux).

Key words: accretion, accretion discs – stars: magnetic fields – stars: neutron – pulsars: general.

1 INTRODUCTION

The magnetic dipole moments μ of neutron stars are observed to decrease with accreted mass, $M_{\rm a}$. Evidence of this trend is found in a variety of systems, e.g. low- and high-mass X-ray binaries, and binary radio pulsars with white dwarf and neutron star companions (Taam & van den Heuvel 1986; Shibazaki et al. 1989; van den Heuvel & Bitzaraki 1995), although there is some debate over whether the trend is monotonic (Wijers 1997). Several theoretical mechanisms have been proposed to explain the $\mu(M_{\rm a})$ data, including accelerated Ohmic decay (Urpin & Geppert 1995; Urpin & Konenkov 1997), fluxoid–vortex interactions (Muslimov & Tsygan 1985; Srinivasan et al. 1990) and magnetic screening or burial (Bisnovatyi-Kogan & Komberg 1974; Romani 1990). With regard to the latter mechanism, Payne & Melatos (2004) (hereafter PM04) calculated a sequence of two-dimensional, hydromagnetic (Grad–Shafranov) equilibria describing the structure of the magnetically confined mountain of material accreted at the magnetic poles of the neutron star. The mountain is confined by magnetic stresses near the equator, where the field is compressed (Melatos & Phinney 2001). These solutions are the first of their kind to explicitly disallow cross-field transport of material as the mountain evolves from its initial to its final state (cf. Mouschovias 1974), as required in the ideal-magnetohydrodynamic (ideal-MHD) limit. PM04 found that μ is screened substantially above a critical accreted mass $M_{\rm c} \sim 10^{-5}\,{\rm M}_{\odot}$, well above previous estimates of $M_{\rm c} \lesssim 10^{-10}\,{\rm M}_{\odot}$ (Hameury et al. 1983; Brown & Bildsten 1998; Litwin, Brown & Rosner 2001).

PM04 calculated equilibria up to $M_{\rm a} \lesssim 10^{-4}\,{\rm M}_{\odot}$, falling short of the mass required ($\sim$0.1 $\,{\rm M}_{\odot}$) to spin up a neutron star to millisecond periods (Burderi et al. 1999). This is supplied by a large class of mass donors like low-mass X-ray binaries (LMXBs) (Strohmayer & Bildsten 2006), even given non-conservative mass transfer (Tauris, van den Heuvel & Savonije 2000). Grad–Shafranov calculations are stymied above $M_{\rm a} \sim 10^{-4}\,{\rm M}_{\odot}$ by physical effects (e.g. magnetic bubbles form above the stellar surface) and numerical effects (e.g. steep magnetic gradients hinder iterative convergence). In this paper, we extend the $\mu(M_{\rm a})$ relationship to $M_{\rm a} \sim 10^{-3}\,{\rm M}_{\odot}$ by loading equilibria with $M_{\rm a} \sim 10^{-4}\,{\rm M}_{\odot}$ into ZEUS-3D, a multipurpose time-dependent, ideal-MHD code for astrophysical fluid dynamics, and adding extra mass quasi-statically through the outer boundary of the simulation volume.

PM04 also left open the important question of the stability of the hydromagnetic equilibria. Distorted magnetic configurations, in which the polar flux is buried beneath the accreted overburden and compressed into a narrow belt at the magnetic equator, are expected prima facie to be unstable. Indeed, the Grad–Shafranov analysis in PM04 hints at the existence of an instability by predicting

★E-mail: dpayne@physics.unimelb.edu.au

(informally) the existence of magnetic bubbles as steady-state solutions. In this paper, we systematically explore the stability of the equilibria by evolving them in ZEUS-3D, subject to linear and non-linear perturbations.

The structure of the paper is as follows. In Section 2, the necessary theory is summarized and the solution method described. The formalism of PM04 is again used here. The numerical Grad–Shafranov solver is described in appendix B of PM04 and appendix C of Mouschovias (1974). In Section 3, we verify ZEUS-3D against a set of test cases relevant to the problem of magnetic burial; the implementation is described thoroughly in Appendix A. In Section 4, we explore the late stages of magnetic burial ($10^{-5} \lesssim M_{\rm a}/{\rm M}_\odot \lesssim 10^{-3}$) by adding mass quasi-statically to equilibria from PM04 in ZEUS-3D. In Section 5, we discuss the linear and non-linear stability of the equilibria in the regime $10^{-5} \lesssim M_{\rm a}/{\rm M}_\odot \lesssim 10^{-3}$. The paper concludes, in Section 6, with a discussion of the limitations of our analysis and suggestions for future numerical work.

2 PHYSICS OF MAGNETIC BURIAL

2.1 Axisymmetric equilibria

During accretion on to a neutron star from a binary companion, matter piles up on the polar cap, funnelled by the magnetic tension of the polar magnetic flux tube. Once $M_{\rm a}$ exceeds $\sim 10^{-5}\,{\rm M}_\odot$, the hydrostatic pressure at the base of the accretion column overcomes the magnetic tension and matter spreads over the stellar surface towards the equator, dragging along frozen-in polar field lines (PM04). The distorted magnetic field leads to screening currents which act to decrease the magnetic dipole moment. Fig. 1(a) illustrates the magnetic 'tutu' formed for $M_{\rm a} = 10^{-5}\,{\rm M}_\odot$, cut-off at 10 density scale-heights. The polar mountain of accreted material (dashed contours) and the pinched, flaring, equatorial magnetic belt (solid contours) are plainly seen.

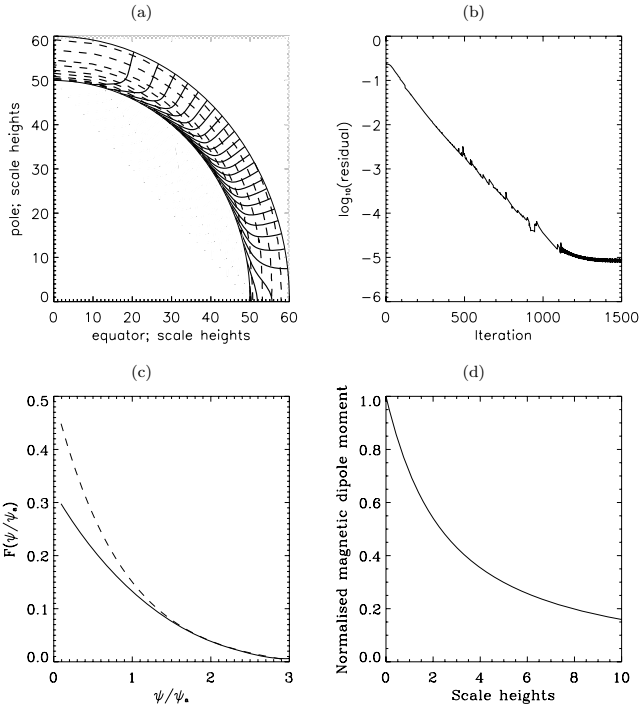

Figure 1. Hydromagnetic equilibrium for $a = 50$ (scaled from real stellar dimensions as discussed in Section 3.3) and $M_{\rm a}/M_{\rm c} = 0.16$, with $G_x = G_y = 64$, showing (a) magnetic field lines (solid) and density contours (dashed) and (b) the corresponding mean residual versus iteration number for an underrelaxation parameter $\Theta = 0.99$. (c) Final $F(\psi)$ (solid) and initial $F(\psi)$ (dashed) versus ψ. (d) Magnetic dipole moment (normalized by its surface value) as a function of altitude above the stellar surface (in units of h_0).

At first glance, one might expect such equilibria, with their steep density and magnetic field gradients, to be unstable. Interestingly, this expectation is largely false, as we show in Section 5. We summarize the key equations and notation of magnetic burial here (PM04).

The steady-state ideal-MHD equations for an isothermal atmosphere ($p = c_{\rm s}^2\rho$, i.e. adiabatic index $\gamma = 1$) reduce to the force equation $\nabla p + \rho\nabla\phi - \mu_0^{-1}\,(\nabla\times\boldsymbol{B})\times\boldsymbol{B} = 0$. For an axisymmetric configuration in spherical polar coordinates (r, θ, ϕ), a flux function $\psi(r, \theta)$ generates the magnetic field $\boldsymbol{B}$ via $\boldsymbol{B} = \nabla\psi(r,\theta)/(r\sin\theta)\times\hat{\boldsymbol{e}}_\phi$. The flux function satisfies the Grad–Shafranov equation

$$\Delta^2\psi = F'(\psi)\exp\left[-(\phi-\phi_0)/c_{\rm s}^2\right], \tag{1}$$

where ρ, p, ϕ, ϕ_0, $c_{\rm s}$ and Δ^2 denote the matter density, pressure, gravitational potential, surface gravitational potential, sound speed and Grad–Shafranov operator, respectively (PM04). In the limit $h_0 = c_{\rm s}^2R_*^2/(GM_*) \ll R_*$, $\phi = GM_*r/R_*^2$, where M_* is the mass of the neutron star and R_* is its radius, mass-flux conservation in ideal-MHD provides the integral constraint

$$F(\psi) = c_{\rm s}^2\frac{{\rm d}M}{{\rm d}\psi} \times\left\{2\pi\int_C {\rm d}s\, r\sin\theta|\nabla\psi|^{-1}\exp\left[-(\phi-\phi_0)/c_{\rm s}^2\right]\right\}^{-1}. \tag{2}$$

We prescribe the mass-flux distribution to be ${\rm d}M/{\rm d}\psi = (M_{\rm a}/2\psi_{\rm a})\exp(-\psi/\psi_{\rm a})$, where $\psi_{\rm a} = \psi_* R_*/R_{\rm a}$ is the flux enclosed by the inner edge of the accretion disc at a distance $R_{\rm a}$ and ψ_* is the hemispheric flux. For the boundary conditions, we fix ψ to be dipolar at $r = R_*$, assume north–south symmetry, fix the $\psi = 0$ field line, and leave the field free at large r.

Equations (1) and (2) are solved numerically using an iterative relaxation scheme (Mouschovias 1974; PM04). The mean residual as a function of iteration number is shown in Fig. 1(b), corresponding to the Grad–Shafranov equilibrium for $m = M_{\rm a}/M_{\rm c} = 0.16$ displayed in Fig. 1(a). The form of $F(\psi)$, found from (2), varies from $M_{\rm a} = 0$ to $M_{\rm a} = 0.16M_{\rm c}$ in the manner displayed in Fig. 1(c).

2.2 Critical accreted mass $M_{\rm c}$

According to naive estimates based on hydromagnetic force balance between $\mu_0^{-1}(\nabla\times\boldsymbol{B})\times\boldsymbol{B}$ and ∇p at the polar cap, the magnetic field (and hence μ) is distorted appreciably away from its initial configuration for $M_{\rm a} \geqslant M_{\rm c} \sim 10^{-8}\,{\rm M}_\odot$ (Brown & Bildsten 1998; Litwin et al. 2001). However, self-consistent solutions of (1) and (2), in which mass does not migrate across flux surfaces and the back reaction from equatorial magnetic stresses is included (PM04), predict a larger value of $M_{\rm c}$, given by

$$\frac{M_{\rm c}}{{\rm M}_\odot} = \pi G M_* B_*^2 R_*^2/\left(2\mu_0 c_{\rm s}^4\,{\rm M}_\odot\right) = 1.2\times10^{-4}\left(\frac{M_*}{1.4\,{\rm M}_\odot}\right)\left(\frac{R_*}{10^4{\rm m}}\right)^2 \times\left(\frac{B_*}{10^8{\rm T}}\right)^2\left(\frac{c_{\rm s}}{10^6\,{\rm m\,s^{-1}}}\right)^{-4}. \tag{3}$$

In the regime $M_{\rm a} \lesssim M_{\rm c}$, the Green function analysis in PM04 gives

$$\psi(r,\theta) = \psi_{\rm d}(r,\theta)[1 - mb^2(1-{\rm e}^{-x/h_0})], \tag{4}$$

with $m = M_a/M_c$ and $b = \psi_*/\psi_a$. The distorted field lines develop a large tangential component as mass is added, such that $|\boldsymbol{B}|$ increases substantially for $M_a \gtrsim M_c/a$, with $a = R_*/h_0$.[1] The self-consistent density distribution associated with (4) is given by

$$\rho(r,\theta) = \rho_0 \tilde{F}[\tilde{\psi}(r,\theta)]e^{-x/h_0} \quad (5)$$

with

$$\tilde{F}(\tilde{\psi}) = \frac{b}{2\pi a^2}\exp(-\tilde{\psi})(1-\tilde{\psi}/b)^{1/2}[J(\tilde{\psi})]^{-1}, \quad (6)$$

where we write $\tilde{F} = Fh_0^3 c_s^2/M_a$, $\rho_0 = M_a/h_0^3$, and $\tilde{\psi} = \psi/\psi_a$, and the form factor satisfies $J(\tilde{\psi}) \approx 1$ to better than 10 per cent for all θ except near the equator, $89.5^\circ \leqslant \theta \leqslant 90^\circ$ (see fig. A1 of PM04). In the small-M_a limit, F is calculated by assuming ψ to be dipolar and evaluating the (small) correction from (1) using Green functions.

2.3 Screening the magnetic dipole

The magnetic dipole moment is defined in terms of the radial component of the magnetic field by

$$\mu = \frac{3}{4}r^3\int_{-1}^{1} d(\cos\theta)\,\cos\theta\, B_r(r,\theta), \quad (7)$$

assuming axisymmetry. In the regime $M_a \lesssim M_c$ from (4), we obtain

$$\mu/\mu_i = (1 - M_a/M_c), \quad (8)$$

where $\mu_i = \psi_* R_*$ is the initial dipole moment. Equation (8) depends only on $m = M_a/M_c$, not M_a and M_c individually, just as in (4). Fig. 1(d) shows how μ decreases as a function of altitude due to the screening currents within the first few density scaleheights. It is very important to note that ψ deviates substantially from its dipole form for $M_a/M_c \gtrsim b^{-2}$, whereas μ deviates from μ_i for $M_a/M_c \gtrsim 1$, which occurs at a much later stage of accretion (because $b \gg 1$ usually).

3 NUMERICAL SIMULATIONS OF MAGNETIC BURIAL

Distorted MHD equilibria like the one pictured in Fig. 1(a) are notoriously unstable. In this section, we describe how the astrophysical MHD code ZEUS-3D can be used to investigate the stability of our equilibria. We discuss the set up of ZEUS-3D in Section 3.1 and Appendix A, some verification experiments in Section 3.2 and Appendix A, and the curvature rescaling required to render the magnetic burial problem tractable in Section 3.3.

3.1 ZEUS-3D

ZEUS-3D is a multipurpose, time-dependent, ideal-MHD code for astrophysical fluid dynamics which uses staggered-mesh finite differencing and operator splitting in three dimensions (Stone & Norman 1992a). In this paper, we restrict the dynamics to two dimensions, disabling the third, but employ a spherical polar grid, appropriate for an axisymmetric stellar atmosphere. Previous numerical work focused on the magnetic poles of the accreting star (Brown & Bildsten 1998; Cumming, Zweibel & Bildsten 2001); here, by contrast, equatorial magnetic stresses are treated fully by simulating a complete hemisphere. The density and magnetic field strengths are read into ZEUS-3D from the output of our Grad–Shafranov code (PM04). The time-step Δt_Z is set by the Courant condition satisfied by the fastest MHD wave modes. Details regarding the parameters, initial conditions, boundary conditions, verification tests and coordinate choices in the runs are given in Appendix A.

3.2 Verification

Before implementing the burial problem in ZEUS-3D, we ran a sequence of simpler verification cases.

First, we reproduced the classical results for the non-linear evolution of the Parker instability of a plane-parallel field in rectangular geometry (Mouschovias 1974). We achieved agreement on the minimum stable wavelength $\lambda_{crit} = 4\pi h_0[B^2/(4\pi p) + 1]^{-1/2}$ and reproduced the final, non-linearly evolved equilibrium state to an accuracy of 5 per cent.

Secondly, to test spherical coordinates in ZEUS-3D, we studied the evolution of a spherical isothermal atmosphere containing zero magnetic field, followed by an atmosphere containing a dipolar magnetic field; both of these states are analytic force-free equilibria [$(\nabla \times \boldsymbol{B}) \times \boldsymbol{B} = 0$)]. ZEUS-3D confirmed that these are indeed equilibria; they do not alter significantly even after several thousand Alfvén times. The condition at the outer boundary $r = r_m$ is chosen to suit the problem at hand. The outflow condition leaves the magnetic field free but allows some mass loss, which we minimize by keeping r_m large, to prevent the atmosphere from evaporating over long time-scales. The inflow condition artificially pins the magnetic field, thereby introducing a radial magnetic field at the outer boundary which increases μ artificially when integrated at r_m. It is used at an intermediate stage in the bootstrap algorithm (described in Section 4.2) when adding mass in the $M_a \gg M_c$ regime.

3.3 Curvature rescaling

The characteristic radial (h_0) and latitudinal (R_*) length-scales are very different in a neutron star, creating numerical difficulties which must be handled by rescaling the problem. For a typical neutron star with $c_s = 10^6$ m s^{-1} (Brown & Bildsten 1998), we find $h_0 = 0.54$ m, $a = R_*/h_0 = 1.9 \times 10^4$ and $\tau_0 = h_0/c_s = 5.4 \times 10^{-7}$ s, where τ_0 is the sound crossing time over a hydrostatic scaleheight.

Two input parameters are varied in the simulations: M_a and b. In the regime $M_a \lesssim M_c$, where (4) holds, ψ and consequently μ depend only on $m = M_a/M_c$ and not explicitly on M_a, suggesting that we can artificially reduce $a = R_*/h_0$ by reducing M_* and R_*, as long as we keep $h_0 \propto R_*^2/M_*$ fixed. This has the advantage that the minimum density increases as a decreases (because the atmosphere extends further), decreasing the Alfvén speed and hence increasing the ZEUS-3D time-step Δt_Z. We set $a = 50$, a good compromise that ensures $a \gg 1$ (as for a realistic star) while keeping the computational burden reasonable. This choice corresponds to a model star with $M'_* = 10^{-5}\,M_\odot$ and $R'_* = 27$ m. Our numerical results confirm that μ is independent of a (see Section 4.1), as predicted analytically. This is illustrated in Fig. 2, where $\mu(M_a)$ is plotted for several a values; even for $M_a < M_c$, the deviations are less than 10 per cent.

Our ZEUS-3D grid reaches an altitude $x_m = r_m - R_* = 10\,h_0$ (cf. $>10^3\,h_0$ in PM04). We adopt a restricted domain for two reasons: (i) to maximize grid resolution near the surface of the star, where gradients are steepest; and (ii) to stop the time-step, Δt_Z, from becoming so small that run time and numerical dissipation become excessive (as discussed in Appendix A). According to the Courant condition, Δt_Z scales as $v_{A,max}^{-1} \propto \rho_{min} \propto e^{-x_m/h_0}$. Note that the pole-to-equator sound and Alfvén crossing times (ah_0/c_s and ah_0/v_A, respectively) also decrease as a decreases.

[1] The extra factor of a comes from differentiating ψ with respect to θ.

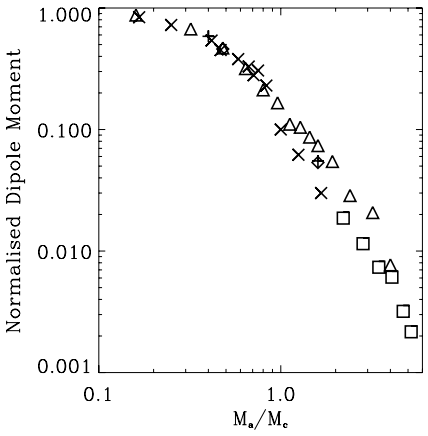

Figure 2. Magnetic dipole moment, μ, as a function of accreted mass, $m = M_a/M_c$, for $b = R_a/R_* = 3$ and $a = R_*/h_0 = 1.86 \times 10^4$ (crosses), $a = 50$ (triangles), $a = 100$ (pluses), $a = 500$ (diamonds), all found with the Grad–Shafranov code and $a = 50$ with mass added through the outer boundary in ZEUS-3D (squares).

4 LATE STAGES OF MAGNETIC BURIAL ($M_a \gg M_c$)

In this section, we investigate the evolution in time of the highly distorted Grad–Shafranov equilibria that arise for $M_a \gg M_c \sim 10^{-4}\,M_\odot$. We aim to answer a question on which the Grad–Shafranov analysis is silent: what happens when significantly more than $10^{-4}\,M_\odot$ is accreted at a rate that is slow compared with the Alfvén time and instability oscillation period (see Section 5)? To do this, we employ the bootstrap approach described in Section 4.2.

4.1 μ versus M_a

Our numerical results confirm that the magnetic dipole moment is essentially independent of $a = R_*/h_0$. Fig. 2 displays $\mu(M_a)$ for several a values, with $M_a > M_c$ achieved by adding mass through the outer boundary of the simulation box (squares). As predicted analytically, there is negligible dependence on a for $M_a < M_c$. For $M_a > M_c$, deviations of less than a factor of 2 occur. The outer boundary condition (radial $\boldsymbol{B}$) artificially increases μ, integrated at $x_m = 10h_0$, by about 10 per cent; this is considered further below [see Fig. 3(f), where μ is plotted as a function of altitude x (dotted curve) for $m = 0.16$]. Hence the magnetic dipole moment plotted in Fig. 2 is an upper bound.

Errors are $\lesssim$1 per cent when compared against other runs with $x_m > 10h_0$. For example, for $m = 0.16$ and $G_x = G_y = 128$, the minimum dipole moment is 0.8695 at $\tilde{x}_m = 10$ and 0.8555 at $\tilde{x}_m = 20$. (A 64×64 grid gives similar results, e.g. $\mu = 0.875$ at $\tilde{x}_m = 10$.)

4.2 Bootstrap accretion: $M_a \gg M_c$

The data in Fig. 2 extend to $M_a \approx 5M_c$, yet the Grad–Shafranov code only produces equilibria for $M_a \lesssim 10^{-4}\,M_\odot$, and breaks down when magnetic bubbles first appear at $M_a \gtrsim M_c b^{-1}$ (Section 4.3). This state of affairs is unsatisfactory because, in many real accreting systems (e.g. LMXBs), M_a exceeds substantially the critical mass for bubbles to form (Taam & van den Heuvel 1986; van den Heuvel & Bitzaraki 1995). For such systems, the previous calculations are useful for the early stages of accretion, at $\tau_a = M_a/\dot{M}_a \leqslant 10^4 b^{-1}$ yr, but teach us little about the final stages of accretion and hence the relic magnetic structure once accretion stops.

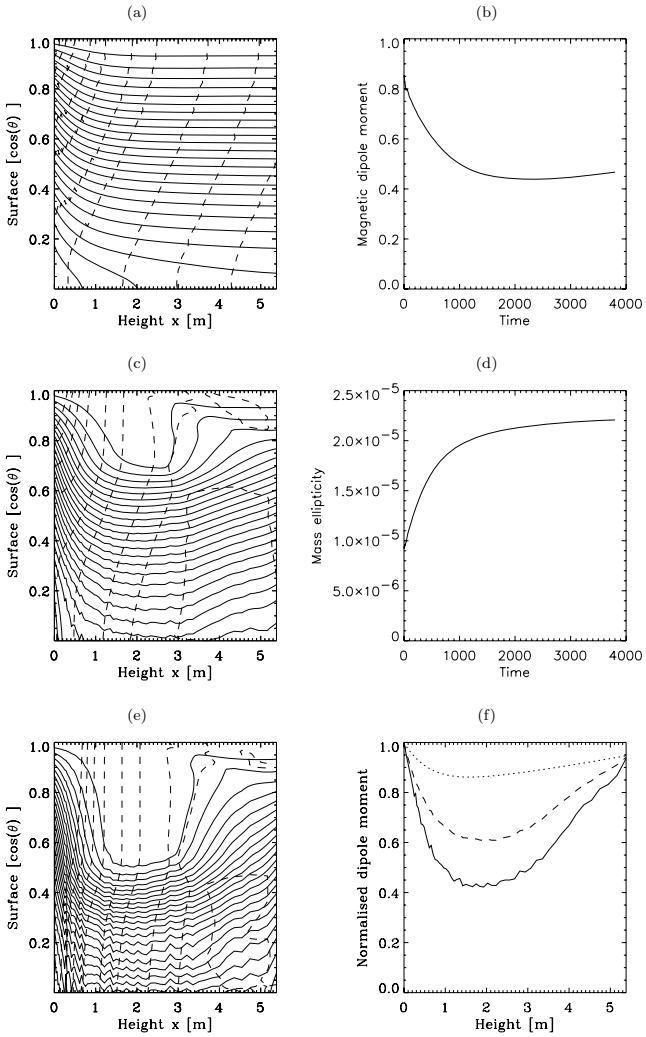

Figure 3. Magnetic field evolution with mass added to the outer boundary. (a), (c), (e): Magnetic field lines (solid) and density contours (dashed) for $t = 0$, 500, 2000, corresponding to $m = 0.16, 0.22, 0.4$, respectively. (b) Dipole moment as a function of time, measured at 3-m above the stellar surface. (d) Quadrupole moment as a function of time. (f) Dipole moment as a function of height for $t = 0$ (dotted), 500 (dashed) and 2000 (solid).

In this section, we perform a numerical experiment to address this issue. We begin with a hydromagnetic equilibrium configuration for ρ and ψ where M_a is just below the critical value for bubbles, calculated using the previous Grad–Shafranov method (PM04). We load this configuration into ZEUS-3D. We then add mass on the polar flux tube $0 \leqslant \psi \leqslant \psi_a$, at a rate slower than all the hydromagnetic time-scales involved in the process of coming to equilibrium (including the Alfvén time-scale and the period of the global Parker oscillations discussed in Section 5), but at a rate faster than the true accretion rate $\dot{M}_a$ (so as to make the computation tractable). We then see what final magnetic structure we get after a realistic amount of mass is accreted, e.g. $M_a \sim 0.1\,M_\odot$ for LMXBs.

This approach does not track properly any processes that operate on time-scales between τ_A and τ_A, such as Hall drift (Cumming, Arras & Zweibel 2004) and Ohmic diffusion (Romani 1990). However, it does model all time-dependent ideal-MHD effects in the context of polar magnetic burial for the first time. Note that this experiment would be completely impractical without the Grad–Shafranov

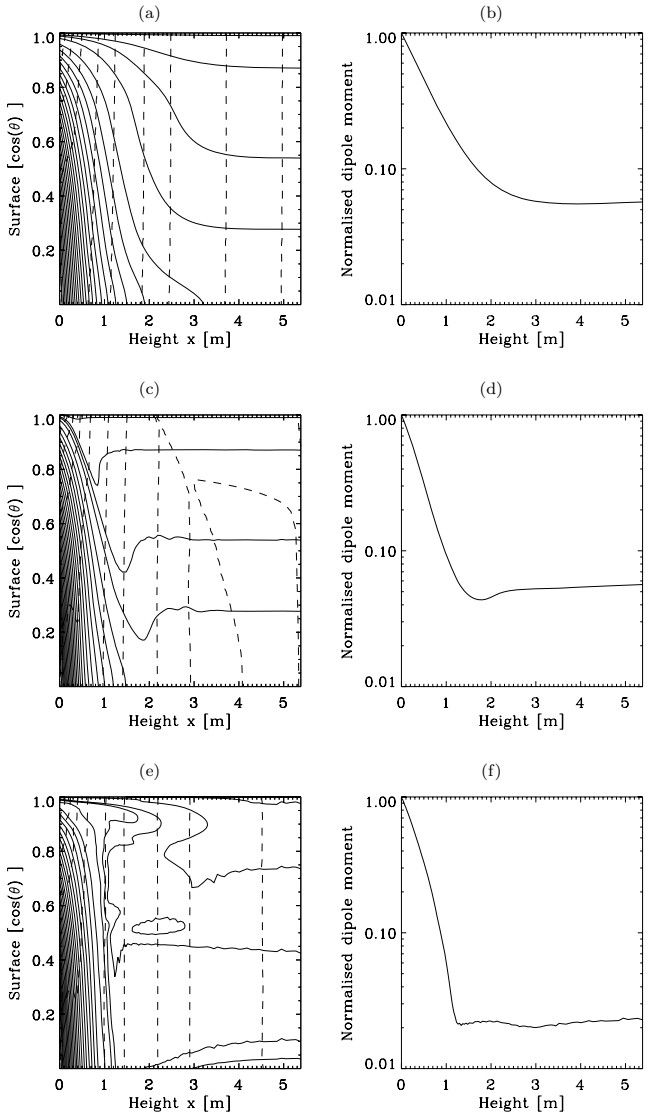

Figure 4. Illustration of one step in the bootstrapping algorithm. Magnetic field lines (solid) and density contours (dashed) (left) and the magnetic dipole moment as a function of height (right) for $m = 1.6$ at $t = 0$ (top), $m = 2.2$ at $t = 100$ (middle), reached by adding mass at the outer boundary, and $m = 4.1$ at $t = 400$ (bottom).

equilibria previously computed for $M_a b \lesssim 10^{-4}\,\mathrm{M}_\odot$ (PM04), because the separation of the hydromagnetic and accretion time-scales is too great if one starts from $M_a = 0$, even when the accretion is accelerated artificially.

Fig. 4 illustrates one bootstrapping cycle; it is also a good illustration of the dynamics of magnetic burial for $M_a \gg M_c$. Starting from a steady-state equilibrium with $m = 1.6$, we add mass to the outer boundary, with inflow boundary conditions. The magnetic field lines are tied to the outer boundary by this condition in ZEUS-3D, preventing μ from decreasing there and raising μ artificially closer to the star. To overcome this, we change the outer boundary condition from inflow (***B*** pinned) to outflow (***B*** free) after adding progressively more mass through the polar flux tube, with $\dot{M}_a(\theta) = \dot{M}_{a,\max} e^{-b\sin^2\theta}$ and $\dot{M}_{a,\max} \approx 2 \times 10^{-6}\,\mathrm{M}_\odot/\tau_0$ when scaled up from the model ($a = 50$) to a realistic neutron star. Mass falls along field lines [Fig. 4(a)] towards the stellar surface and flattens the equatorial 'tutu', until the magnetic tension matches the hydrostatic pressure. Matter subsequently flows equatorward, dragging magnetic field lines with it [Fig. 4(c)]. Superposed on this process are sound and Alfvén oscillations, which are discussed in Section 5; they cause wiggles in the field lines, visible above the spreading matter (2–3 m above the surface). The oscillations show up clearly in the time evolution of the magnetic dipole moment, and mass quadrupole moment, plotted in Fig. 5. [Further discussion of the mass distribution appears in Melatos & Payne (2005).] Finally, the mass inflow is stopped and the outer boundary condition is switched to outflow, allowing the magnetic field lines to relax [Fig. 4(e)]. The configuration in Fig. 4(e) becomes the initial state for further mass to be added.

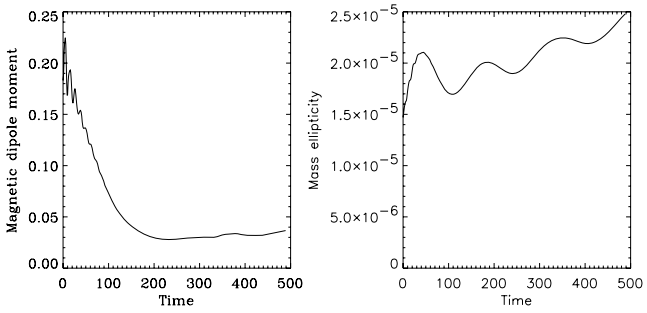

Figure 5. Evolution of the magnetic dipole moment, as measured 1.5-m above the stellar surface (left-hand panel), and the mass ellipticity (right-hand panel), when mass is added to a $m = 0.16$ equilibrium.

The dipole moment attained after adding a total of $3 \times 10^{-4}\,\mathrm{M}_\odot$ on a 128×128 grid is shown in Fig. 6 as a function of altitude. We find that a minimum dipole moment of $\approx 3 \times 10^{-3}$ times the surface value is obtained for $m = 4.76$ at an altitude $\sim h_0$. Smaller dipole moments are expected for larger M_a, but numerical constraints prevented us from improving the grid resolution nearer the equator sufficiently to see this.

One might be tempted to ask whether the intermediate step of relaxing the field at r_m is really necessary. It is, and Figs 3 and 4 illustrate why. If too much mass is added, it is found numerically that the field lines break off the underlying magnetic dipole and, when allowed to relax, remain pinned to the outer boundary. Fig. 5 shows μ as a function of time, measured $\sim$1.5 m above the stellar surface where the spreading mostly occurs. μ reaches a minimum after $\sim 100\tau_0$, even when more mass is added, because of line-tying at r_m. Adding more mass is ineffective because closed magnetic loops

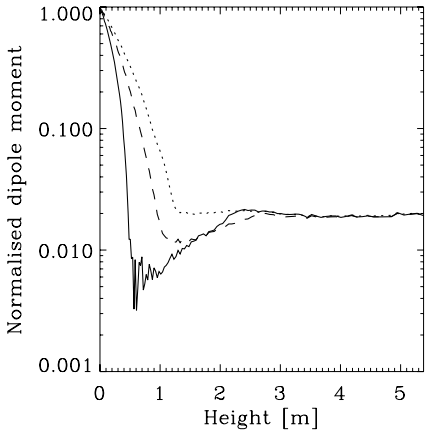

Figure 6. Dipole moment versus altitude when mass is added to the configuration in Fig. 4(c), at $t = 0$ (dotted), $t = 100$ (dashed) and $t = 500$ (solid), corresponding to $m = 2.23, 2.86$ and 4.76, respectively.

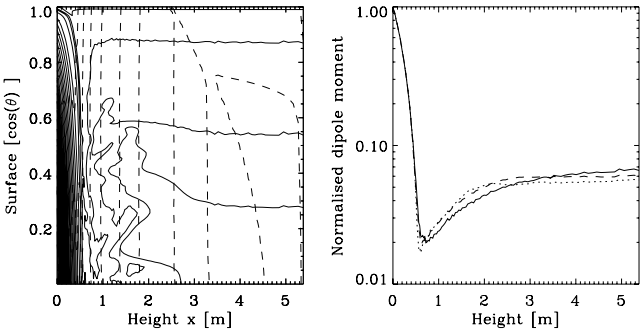

Figure 7. Left-hand panel: magnetic field lines (solid) and density contours (dashed) when mass is added to a $m = 0.16$ equilibrium, reaching $m = 4.1$ at $t = 400$. Right-hand panel: magnetic dipole moment as a function of altitude when the $m = 4.1$ configuration at $t = 0$ (dotted) relaxes in the presence of an outflow outer boundary condition, at $t = 500$ (dashed) and $t = 900$ (solid).

form. They are apparent in Fig. 7, which shows the configuration at $t = 400$ (starting from the $m = 1.6$ equilibrium). This configuration cannot be used as the initial state for the next bootstrapping iteration because the magnetic field lines remain fixed at the outer boundary.

To validate the bootstrapping method, we take an equilibrium that is free of magnetic bubbles (i.e. $m \ll 1$) and add mass up to a value of M_a for which the Grad–Shafranov equilibrium is already known. Generally speaking, we reproduce the Grad–Shafranov value of μ to an accuracy of 5 per cent.

Fig. 3 shows the results of such a test, beginning with $m = 0.16$ and adding mass at a rate $\dot{M}_\mathrm{a}(\theta) = \dot{M}_{\mathrm{a,max}} \mathrm{e}^{-b \sin^2 \theta}$, with $\dot{M}_{\mathrm{a,max}} \approx 7 \times 10^{-8}\,\mathrm{M}_\odot/\tau_0$. We point out several important features. (i) The initial μ in Fig. 3(f) rises towards the outer boundary (see Section 3.2). (ii) μ is unchanged at the outer boundary, because the magnetic field lines are tied there by the flux-freezing condition, to accommodate the inflowing mass. The magnetic field lines bend towards the equator, and μ decreases closer to the stellar surface. (iii) Closer to the surface, μ reaches a minimum within 5 per cent of that obtained from the Grad–Shafranov equilibrium. (iv) The kinks apparent in the magnetic field lines are a result of numerical dissipation on the grid scale.

4.3 Bubbles

When the Grad–Shafranov equation is solved with ψ free (Neumann) at the outer boundary, closed bubbles of magnetic field, disconnected from the inner (Dirichlet) boundary, can arise (PM04) for $M_\mathrm{a} \geqslant 1.6\,M_\mathrm{c}\,b^{-1}$. Physically, they are generated when the toroidal screening current exceeds a threshold. However, the field lines are deformed continuously from a simply connected initial state (e.g. a dipole, or something close to it is the best guess for a typical neutron star) in ideal-MHD. Therefore, the bubbles are not realizable in an accreting neutron star even though they are admissible mathematical solutions to the steady-state boundary-value problem. Instead, the bubbles point to a loss of equilibrium, analogous to that which occurs during eruptive solar phenomena (Klimchuk & Sturrock 1989), where no simply connected hydromagnetic equilibrium exists. In the language of the Grad–Shafranov analysis in Section 2, the source term $\propto F'(\psi)$ in (1) increases with $M_\mathrm{a}\,b$, boosting $\Delta^2\psi$ and creating flux surfaces with $\psi < 0$ or $\psi > \psi_*$, which cannot connect to the star and either form closed loops or are anchored at infinity (here, the accretion disc).

How does a bubble evolve in ZEUS-3D? We import a Grad–Shafranov equilibrium for $M_\mathrm{a} = 1.6 M_\mathrm{c}$ into ZEUS-3D, retaining the

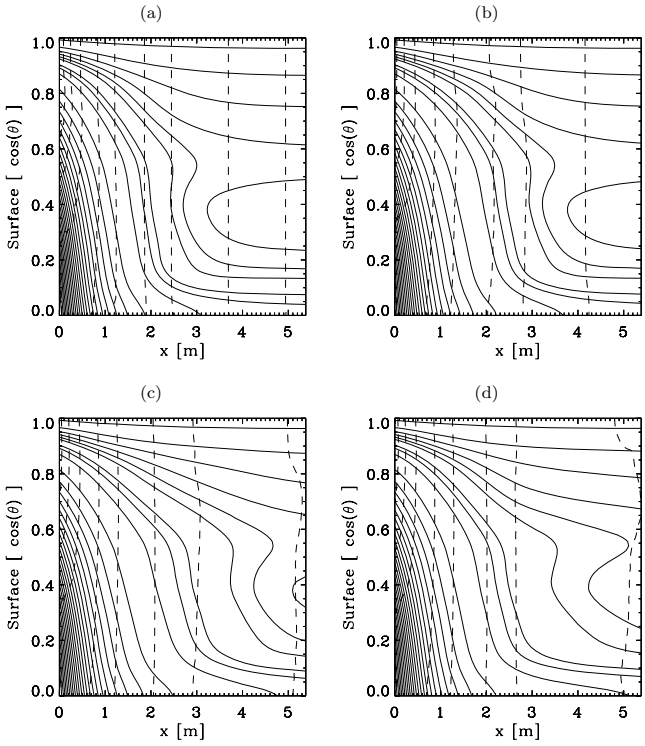

Figure 8. Evolution of a bubble [found initially in the region $3 \leqslant x \leqslant 5$ m, $0.2 \leqslant \cos(\theta) \leqslant 0.5$ in (a)] with $m = 1.6$ initially, after the density is increased uniformly to $m = 3.2$ at $t = 0$. Snapshots are plotted at (a) $t = 0$, (b) $t = 3$, (c) $t = 6$, (d) $t = 9$.

self-consistent density $\rho = F[\psi(r, \theta)]\mathrm{e}^{-x/h_0}$ in the region $0 \leqslant \psi \leqslant \psi_*$ but replacing it with an isothermal atmosphere inside the bubble ($\psi < 0$ and $\psi > \psi_*$), where strict flux-freezing would imply $\rho = 0$ (matter cannot enter without crossing flux surfaces). Fig. 8 shows part of the evolution for $m = 1.6$. The bubble rises to r_m, during the first Alfvén oscillation of the magnetosphere, at the Alfvén speed. During the bubble's rise, 0.5 per cent of the accreted mass ($4.4 \times 10^{-7}\,\mathrm{M}_\odot$ when converted to realistic neutron star parameters; see Appendix A) is ejected through the outer boundary in one Alfvén time. This compares with thermal evaporation of less than 0.001 per cent in the same time, which occurs naturally given outflow boundary conditions (see Appendix A). For $m > 1.6$, the bubble oscillates about an equilibrium point rather than rising buoyantly.

4.4 Uniform density increase

Another route to computing equilibria with $M_\mathrm{a} > 10^{-4}\,\mathrm{M}_\odot$ is to start from a bubble-free Grad–Shafranov equilibrium with $M_\mathrm{a} < M_\mathrm{c}$ and increase the density uniformly across the grid by some factor (usually $\gg 1$), while leaving the magnetic field unchanged. If we start from the initial dipole ($M_\mathrm{a} = 0$), this kind of numerical experiment is badly controlled; it leads to excessive numerical dissipation and mass loss through $r = r_\mathrm{m}$. However, if we start from $M_\mathrm{a} \sim 10^{-5}\,\mathrm{M}_\odot$, the readjustment is gentler. During the early stages of the readjustment, some classic instances of the Parker instability are observed. For example, Fig. 9 shows how the initial state for $m = 1.12$ evolves after the density is increased five-fold uniformly to $m = 5.6$. The magnetic field component B_θ is compressed in the r direction on an Alfvén time-scale – ripe conditions for the Parker instability. The blistering becomes clear after 160 Alfvén times (third frame). After

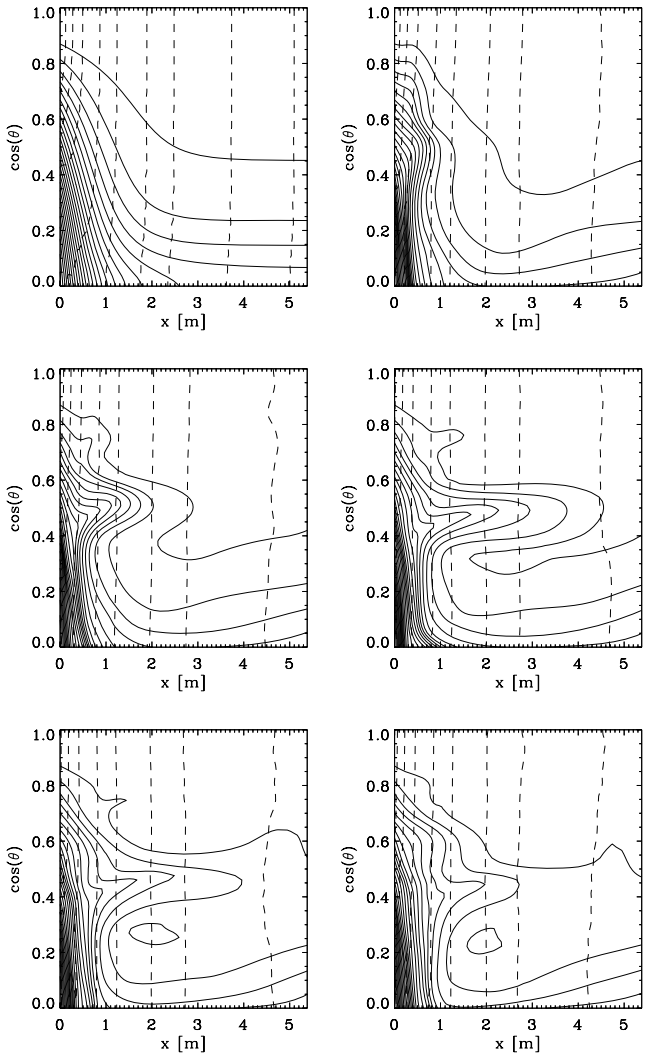

Figure 9. Evolution of the Parker instability for $M_a = 1.12M_c$ with the density increased uniformly across the grid by a factor of 5. Snapshots of the magnetic field lines are shown at $t = 0$, 120, 160, 200, 240 and 280 Alfvén times (top left to bottom right).

280 Alfvén times, the material settles down to a new equilibrium. Importantly, negligible mass and magnetic flux (less than 1 per cent of the total) is lost through this blistering.

The magnetic dipole moment μ, plotted in Fig. 10, settles down to $\approx 0.06\mu_i$. This is larger than we expect for $m = 5.6$, given that we found $\mu(m = 4.7) < 0.01$ using the bootstrapping method. Two factors explain this: (i) the sudden density increase does not allow the magnetic field and matter to gradually find their equilibria, and (ii) flux-freezing is violated by increasing the density as above. This method can be used in conjunction with bootstrapping with less severe density increases (factor of $\ll 5$).

4.5 Size of the polar cap

In our numerical experiments, we choose the polar cap radius to be relatively large because (i) it helps the Grad–Shafranov solution converge numerically while still capturing the essential idea of a polar mountain, (ii) it raises the minimum density $\rho_{\min} \propto e^{-b}$ on the grid, preventing Δt_Z from becoming too small via the Courant condition, and (iii) in a real star, the polar plasma flow can spread

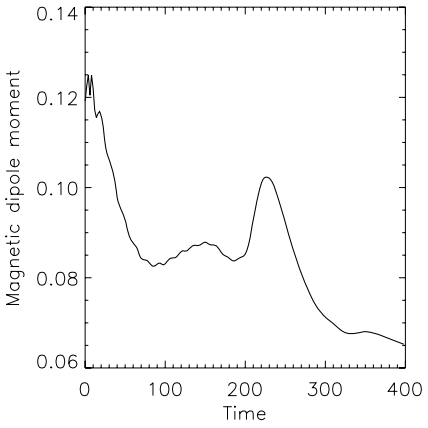

Figure 10. Magnetic dipole moment as a function of time during the blistering of the Parker instability displayed in Fig. 9.

due to Rayleigh–Taylor and Kelvin–Helmholtz instabilities (Arons et al. 1984). We have not managed to get ZEUS-3D running for $b \gg 3$. For $b = 3$ and 5, μ reaches an equilibrium value in a few hundred Alfvén times, and the oscillation frequencies are roughly the same, with $\mu/\mu_i \to 0.85, 0.82$ for $b = 3, 5$ as $t \to$ inf.

4.6 Equatorial magnetic belt

Melatos & Phinney (2001) predicted that the magnetic field at the equator intensifies during magnetic burial, if magnetic flux is conserved. The results presented here confirm this. As seen in Fig. 1(a), the magnetic field is 'combed' away from the pole, and flattened against the stellar surface towards the equator, increasing B_θ at the expense of B_r. The maximum magnetic field strength, $B_{\max}$, is given as a function of M_a in Payne & Melatos (2006b). Note that the analytic approximation in the limit of small M_a captures the equatorial belt provided that $J(\psi)$ is calculated properly (PM04).

5 STABILITY

In this section, we investigate whether the Grad–Shafranov equilibria of magnetically confined mountains calculated in this paper ($M_a \gtrsim M_c$) and PM04 ($M_a \lesssim M_c$) are stable to small and large perturbations. To do this, we load the numerical output from our Grad–Shafranov code into ZEUS-3D, evolve it forward in time, and report on the nature of any instabilities observed. In ideal-MHD, any instabilities manifest themselves as slow, Alfvén, or fast magnetosonic waves, modified by buoyancy effects in a stratified medium.

We explore the stability of the system in the context of three numerical experiments: (i) we test how the small perturbation evolves, which arises from the numerical error in converting from the Grad–Shafranov to the ZEUS-3D grid (Sections 5.1, 5.2 and 5.4); (ii) we consider the fate of large perturbations (Section 5.5); and (iii) we compare the evolution in ZEUS-3D with the convergence of the Grad–Shafranov algorithm.

5.1 Linear stability: numerical experiment

Equilibria of the kind depicted in Fig. 1(a), where the magnetic field is markedly distorted, are normally expected to be unstable. To assess this here, we track separately the evolution of W_g, W_k and W_B, the gravitational, kinetic and magnetic energies, respectively, as the magnetic mountain evolves in ZEUS-3D. The total energy is

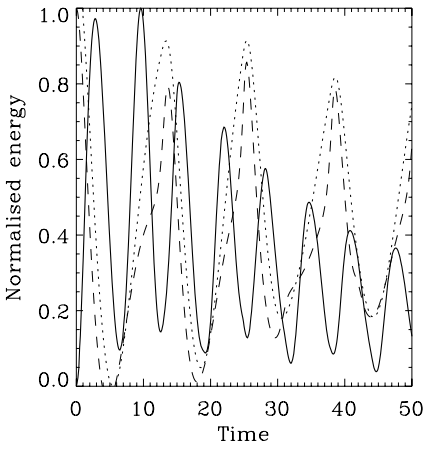

Figure 11. Kinetic (solid), magnetic (dashed) and gravitational potential (dotted) energies, normalized to their maximum values as a function of time for $m = 1.6$, $G_x = G_y = 128$.

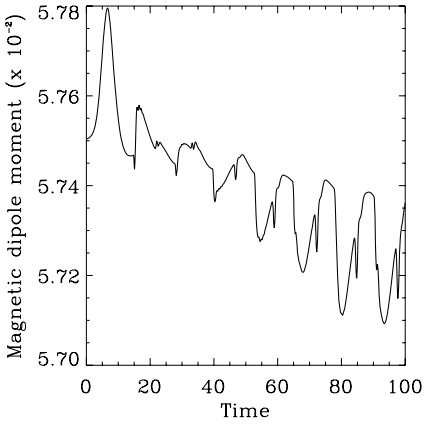

Figure 12. Magnetic dipole moment normalized to its surface value, plotted as a function of time for $m = 1.6$, $G_x = G_y = 128$.

given by

$$W = W_B + W_\mathrm{g} + W_\mathrm{k},$$

where we define

$$W_\mathrm{g} = \int \mathrm{d}^3\boldsymbol{x}\, \rho\phi, \quad W_\mathrm{k} = \int \mathrm{d}^3\boldsymbol{x}\, (\rho v^2/2)$$

and

$$W_B = \int \mathrm{d}^3\boldsymbol{x}\, \left(B^2/2\mu_0\right).$$

Key observables of the system, such as the magnetic dipole moment μ, defined in (7), and the mass ellipticity ϵ, are also tracked. We do not plot the total thermal energy $W_\mathrm{p} = \int \mathrm{d}^3\boldsymbol{x}\, P \log P$ in what follows because ZEUS-3D holds it constant during isothermal (but not adiabatic) runs.

We begin, as an example, with the equilibrium for $m = 1.6$ [Fig. 4(a)], our starting point for adding mass through the outer boundary in Section 4.2. Fig. 11 displays W_g, W_k and W_B a function of t for this case. The energies are normalized by their maximum values so that the energy exchanges are clear, because their absolute values differ by several orders of magnitude: W_g dominates, with $W_B = 3.7 \times 10^{-3} W_\mathrm{g}$ and $W_\mathrm{k} = 4.2 \times 10^{-5} W_\mathrm{g}$ initially. After $300\tau_\mathrm{A}$, we obtain $W_B = 3.4 \times 10^{-3} W_\mathrm{g}$ and $W_\mathrm{k} = 1.2 \times 10^{-5} W_\mathrm{g}$.

The evolution proceeds as follows. The equilibrium state imported into ZEUS-3D is not exact due to grid resolution, imperfect convergence in the Grad–Shafranov code, and numerical discrepancies when translating between the Grad–Shafranov and ZEUS-3D grids (see Appendix A). Initially, during the first oscillation, W_g and W_B are converted to W_k. When the oscillation overshoots, the energy flow reverses direction. In ideal-MHD, where there is no dissipation, the oscillation persists. In ZEUS-3D, where there is some numerical dissipation and energy is radiated by hydromagnetic waves through the outer boundary, the oscillations are damped, as in Fig. 11. However, this damping is slow. (Experiments demonstrating this numerical dissipation are reported in Appendix A.) Note that W_k oscillates at twice the frequency of W_g and W_B, because the leading term in W_k is quadratic in perturbed quantities ($\propto \delta v^2$), whereas $W_\mathrm{g} (\propto \delta\rho)$ and $W_B (\propto B\delta B)$ are linear.

The dipole moment, normalized to its value at the stellar surface, is plotted in Fig. 12 for $m = 1.6$. The oscillation period equals that of W_B for the reason above. The kinks in the curve occur when the magnetic field reflects off the boundaries at the pole and equator. The oscillations are identified as acoustic modes (see Section 5.2).

5.2 Global MHD oscillations

We explore here the physical nature of the oscillations resulting from small perturbations to the hydromagnetic equilibria and how their amplitude and period depend on M_a.

Fig. 13 shows the time evolution of μ and mass ellipticity for several M_a values and logarithmic scaling of the altitude. For reference and numerical comparison, the results for a linear scaling in altitude are shown in Fig. 14. The key result is that the equilibria are marginally stable: the buried field is not disrupted significantly, but the configuration oscillates about its equilibrium state. Two modes are clearly present: (i) a short period oscillation, with fixed period $13\tau_0$ for all M_a (and thus ρ), which is an acoustic mode with velocity c_s; and (ii) a longer period oscillation, with period increasing with M_a as displayed in Fig. 15, which is an Alfvén mode. The Alfvén oscillation frequency is fitted by

$$f_\mathrm{A} \approx 0.003\tau_0^{-1}(M_\mathrm{a}/M_\mathrm{c})^{-1/2}\,\mathrm{Hz} \tag{9}$$

for $a = 50$, which, when scaled to a realistic neutron star, yields

$$f_\mathrm{A} \approx 17(M_\mathrm{a}/M_\mathrm{c})^{-1/2}\,\mathrm{Hz}. \tag{10}$$

There are a few numerical considerations. The magnetic dipole moment artificially rises from its equilibrium value towards the surface value for $0.2 \lesssim m \lesssim 1.6$ under the following conditions. (i) There is insufficient resolution close to the stellar surface, e.g. a linear grid in r with $G_x = 128$ is not good enough. A comparison of Figs 13 (logarithmic r grid) and 14 (linear r grid) brings out this point. μ and the quadrupole moment exhibit oscillations, whose amplitude grows and whose mean varies for a linear grid, whereas the amplitude is damped and the mean remains constant for a logarithmic grid. (ii) The outer boundary condition is set to *outflow*, leading to a small amount of mass loss. While the mass loss amounts to $\lesssim$2 per cent by $t = 10^3$, it allows the field lines at the magnetic equator to flare up towards the pole and destabilize the equilibrium. These problems are overcome by (i) using a logarithmic scale in r to increase the grid resolution near the stellar surface, (ii) managing carefully the translation from logarithmic scaling in the Grad–Shafranov grid to the ZEUS-3D grid (see Appendix A), and (iii) setting the outer boundary condition to *inflow*.

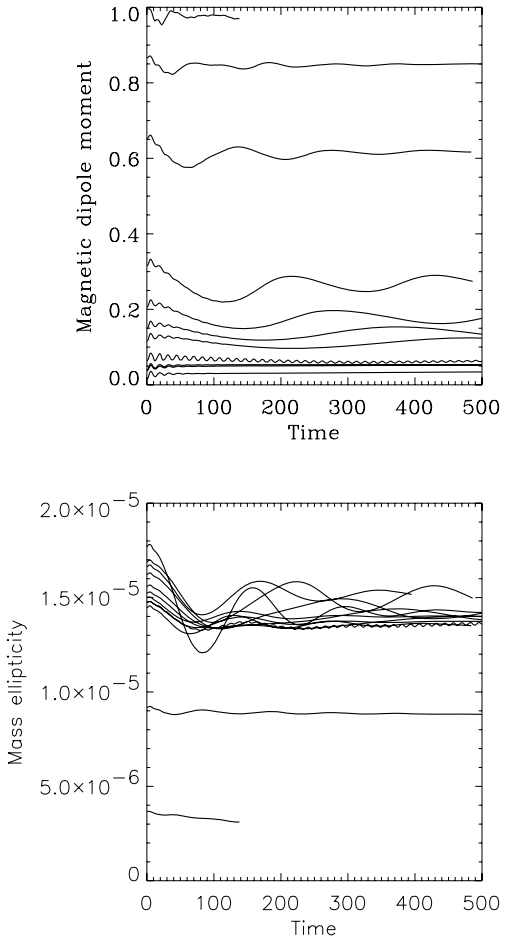

Figure 13. Magnetic dipole moment (top) and mass quadrupole moment (bottom) as a function of time for $M_a/M_c = 0.053$, 0.16, 0.32, 0.48, 0.64, 0.8, 0.96, 1.12, 1.6, 2.4, 3.2 and 4.0 (top to bottom for μ, and bottom to top for the quadrupole moment). Grid resolution: $G_{x,y} = 128$, with logarithmic scaling in altitude.

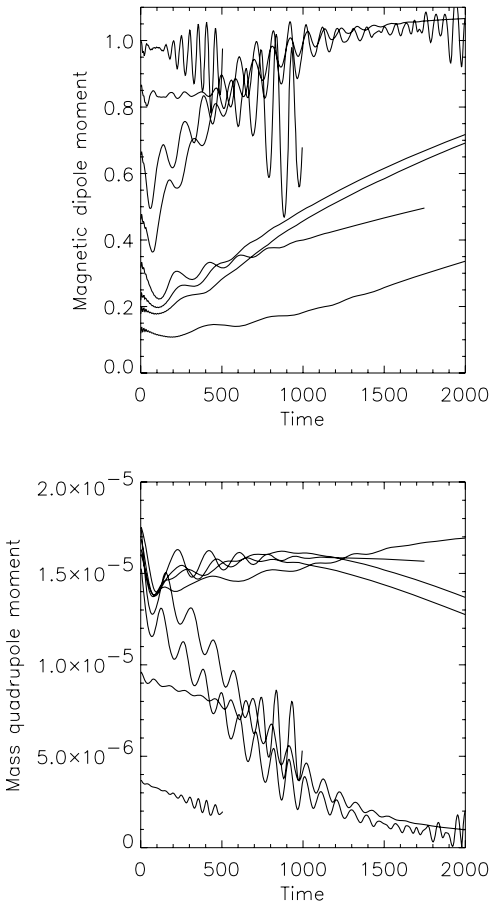

Figure 14. Magnetic dipole moment (top) and mass quadrupole moment (bottom) as a function of time for $M_a/M_c = 0.053$, 0.16, 0.32, 0.48, 0.64, 0.96, 1.12 (top to bottom for μ, and bottom to top for the quadrupole moment). Grid resolution: $G_{x,y} = 64$, with linear scaling in altitude.

5.3 Identifying MHD modes

To classify the oscillation modes discovered in the previous section, we need the dispersion relation of small-amplitude MHD waves in the limit (verified by the simulations) where the wavelength of the ρ and $\boldsymbol{B}$ perturbations is small compared with $|\rho|/|\nabla\rho|$ and $|\psi|/|\nabla\psi|$. The force equation governs stability: intuitively, if a fluid (Lagrangian) displacement $\boldsymbol{\xi}$ creates a force $\boldsymbol{F}$ in the opposite direction, equilibrium tends to be restored and the system is stable. Upon analysing the perturbation in Fourier modes, $\boldsymbol{\xi}(\boldsymbol{r}, t) \propto \boldsymbol{\xi}(\boldsymbol{k}, \omega)\mathrm{e}^{-\mathrm{i}(\boldsymbol{k}\cdot\boldsymbol{r}-\omega t)}$, the force equation reads

$$\rho_0\omega^2\boldsymbol{\xi} = -c_s^2\rho_0\boldsymbol{k}\boldsymbol{k}\cdot\boldsymbol{\xi}(\boldsymbol{k},\omega) + \mu_0^{-1}[\![\{\boldsymbol{k}\times[\boldsymbol{k}\times(\boldsymbol{\xi}\times\boldsymbol{B}_0)]\}\times\boldsymbol{B}_0]\!]. \tag{11}$$

In the Wentzel–Kramers–Brillouin (WKB) limit $k \gg |\nabla\psi|/|\psi|$, the dispersion relation (11) supports two modes: shear Alfvén waves, with

$$\omega^2 = k_\parallel^2 v_A^2, \tag{12}$$

and fast (+) and slow (−) magnetosonic waves, with

$$\omega^2 = \tfrac{1}{2}k^2\left(c_s^2 + v_A^2\right)\left[1 \pm (1-\delta)^{1/2}\right] \tag{13}$$

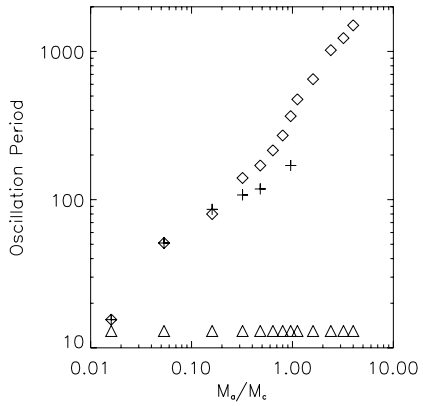

Figure 15. Oscillation period (in units of the Alfvén time) as a function of M_a, with linear (crosses) and logarithmic (diamonds) grid sampling in altitude. The Alfvén period is well fit by $300\tau_0(M_a/M_c)^{1/2}$. The period of the sound mode (triangles) is also plotted. Note that τ_0 is defined at a particular value of M_a.

and

$$\delta = \frac{4k_\parallel^2 c_s^2 v_A^2}{k^2\left(c_s^2 + v_A^2\right)^2}. \tag{14}$$

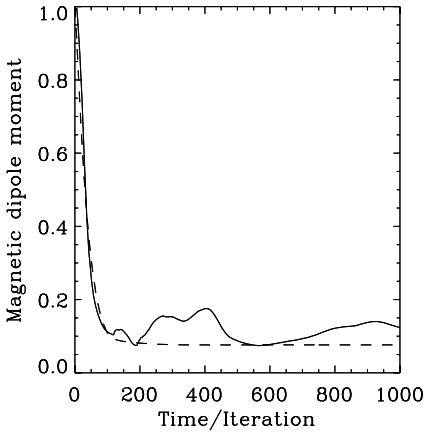

Figure 16. Magnetic dipole moment as a function of time in ZEUS-3D (solid) and as a function of iteration number in the Grad–Shafranov code with underrelaxation parameter $\Theta = 0.99$ (dashed).

The shear Alfvén wave is incompressible ($\boldsymbol{k} \cdot \boldsymbol{\xi} = 0$). It propagates analogously to a transverse wave along a string under tension, the magnetic field lines playing the role of the string.

Let us denote the right-hand side of (11) by $\boldsymbol{F}(\boldsymbol{\xi})$. The operator $\rho^{-1}\boldsymbol{F}$ is linear. It can be shown [see p. 244 of Goedbloed & Poedts (2004) for a proof] that in ideal-MHD, the operator $\rho^{-1}\boldsymbol{F}$ is also self-adjoint, so that the eigenvalues ω^2 in (11) are real (making ω either real or purely imaginary). Two classes of solution occur: (i) stable pure waves ($\omega^2 > 0$) and (ii) exponentially growing instabilities ($\omega^2 < 0$). There are no damped oscillations in ideal-MHD, even in a non-uniform background; any dissipation observed is numerical.

A full theoretical calculation of the two-dimensional stability is beyond the scope of this paper. However, we attempt to interpret the numerical results displayed in equations (9) and (10) in terms of known results for a gravitating, magnetized slab (Goedbloed & Poedts 2004). We assume that the slab is infinite and homogeneous in the y- and z-directions, contained between two planes at $x = x_1$ and $x = x_2$; that the equilibrium ρ and ψ vary in the x-direction; and that the excited modes satisfy the boundary conditions $\xi_x(x_1) = \xi_x(x_2) = 0$. The results for a slab provide insight into the oscillation modes of a neutron star's magnetosphere, where the above boundary conditions are well satisfied due to a combination of line tying at $r = R_*$ and stratification at all r (the component of $\boldsymbol{\xi}$ perpendicular to equipotential surfaces is small). Working with coordinates in a field-line projection, the Alfvén and slow continuum frequencies are estimated to be (Goedbloed & Poedts 2004)

$$\omega_{\rm A}^2 = 4\pi\mu_0^{-1}\rho^{-1}F^2, \quad \omega_{\rm S}^2 = 4\pi\mu_0^{-1}\frac{\gamma p}{\gamma p + 4\pi\mu_0^{-1}B^2}\rho^{-1}F^2 \quad (15)$$

with $F = -\mathrm{i}\boldsymbol{B} \cdot \nabla$. From our numerical simulations, we find empirically that $\approx 1/2$ wavelength of the dominant oscillation mode fits within one quadrant, yielding radial and latitudinal wavenumbers $\sim 2/R_*$. This gives $F \sim 2B_{\rm max}/R_*$ and thus $\omega_{\rm A}^2 = 4B_{\rm max}^2/(R_*^2\rho_{\rm max})$, using the maximum magnetic field strength and density as characteristic values. Empirically, from our simulations, we find $B_{\rm max} \approx 10^9$ T for $M_{\rm a} = M_{\rm c}$, $\rho_{\rm max} \approx 10^{13}(M_{\rm a}/M_{\rm c})\,{\rm kg\,m^{-3}}$, and hence $f_{\rm A} = \omega_{\rm A}/(2\pi) = 32(M_{\rm a}/M_{\rm c})^{-1/2}$ Hz. This scales the same way as the numerical result $f_{\rm A} = 17(M_{\rm a}/M_{\rm c})^{-1/2}$ Hz but is larger, due to the crudeness of our slab approximation and numerical estimates. The plasma varies with density (and $M_{\rm a}$) from being high-β at the stellar surface to low-β far from the star, given that $c_{\rm s}$ is uniform where the mass is concentrated and the waves are launched.

Fig. 15 shows the oscillation period as a function of m. When analysing the MHD evolution, we extract the period of the waves by Fourier analysis in order to distinguish which modes are excited. For the Alfvén mode, as the average density increases (with m), $v_{\rm A} \propto M_{\rm a}^{-1/2}$ decreases, and thus the oscillation period increases. The Alfvén period (in units of the Alfvén time) is fitted by $300\tau_0(M_{\rm a}/M_{\rm c})^{-1/2}$. The period of the acoustic mode remains constant throughout all the simulations we perform.

5.4 Transient Parker instability

In the experiments described in Section 4.4, it is observed that increasing the density uniformly by a factor of $\gtrsim 4$ causes Parker instabilities to occur. Fig. 9 consists of a sequence of frames illustrating the evolution of the Parker instability for an equilibrium state whose density is uniformly increased five-fold. The wavelength λ of the instability subtends ≈ 1 rad, i.e. $\lambda \approx 0.3R_*$. The radial density profile is exponential, while the magnetic field is mostly confined to a layer of thickness $\sim h_0$, directed perpendicular to ∇P. This is the classic situation in which Parker instabilities are expected (Mouschovias 1974).

The evolution of μ, as measured at $x = 10h_0$, is displayed in Fig. 10. Note that, after the Parker blister subsides, μ returns to its original value. The equilibrium is not disrupted permanently; indeed, less than ~ 1 per cent of the accreted layer and frozen-in magnetic flux are expelled from the simulation domain. In this respect, the instability can be considered transient.

The Grad–Shafranov equilibria imported from PM04 are generated by an algorithm that can follow, by successive relaxation, the full non-linear evolution of the Parker instability (Parker 1966; Mouschovias 1974). Therefore it is unsurprising that the equilibria are stable; the relaxation algorithm evolves the magnetic field quasi-statically through a sequence of intermediate 'states' quite close to those that the real solution to the time-dependent MHD equations would pass through. True, the final state is distorted, and one might ask why the buoyancy of the compressed magnetic flux does not drive long-wavelength, slow MHD modes that overturn the accreted matter on the Alfvén time-scale — something that does not occur in the ZEUS-3D runs (except for the transient in Fig. 9). The explanation is that the equatorial magnetic 'tutu' represents the end state of a Parker instability that occurs quasi-statically as we add material. The tutu is the analogue of the stable magnetic 'blisters' which form when the plane-parallel Parker instability saturates, while the polar mountain is the analogue of the material that drains into the magnetic valleys.

To test the assertion (PM04) that the iterative solution of the Grad–Shafranov equation coupled to a flux-freezing condition provides a good proxy for the true time-dependent behaviour, we begin with a magnetic dipole with excess mass loaded into the polar flux tube in both the Grad–Shafranov code and ZEUS-3D. In ZEUS-3D, this is effectively the same as applying a uniform density increase (Section 4.4) to the $m = 0$ equilibrium, ending up with $m = 1.6$ in this example. We plot μ as a function of time (ZEUS-3D) and iteration number (Grad–Shafranov) in Fig. 16. An underrelaxation parameter $\Theta = 0.99$ is selected by trial and error to give a comparable rate of convergence in the two codes. The initial progress to equilibrium is similar in both cases. However, after 100 iterations (or equivalently $t \geqslant 100$), μ fluctuates more in ZEUS-3D than in the converging Grad–Shafranov code. In ZEUS-3D, the added mass initially squashes the field into a layer $\sim 1/4$ the thickness of the equilibrium layer [Fig. 4(a)]. The field then bounces back and transient Parker-like instabilities occur, as we expect (ρ increases by a factor of $\gtrsim 4$). This is best illustrated in Fig. 17, which shows a

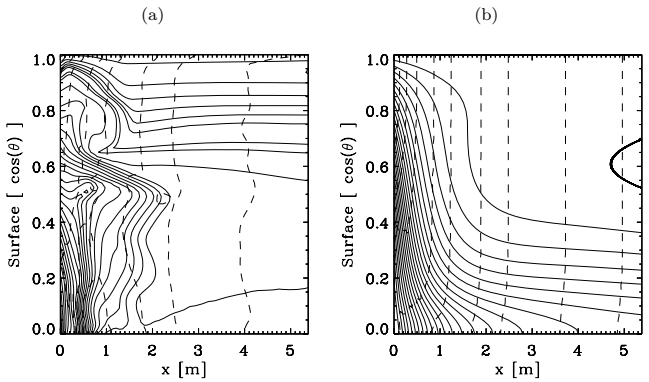

Figure 17. Magnetic field lines (solid) and density contours (dashed) for $t = 100$ in ZEUS-3D (left) and the 100th iteration in the Grad–Shafranov code (right). The initial state is a magnetic dipole with excess mass ($m = 1.6$) in the polar flux tubes ($\psi_*/\psi_a = 3$).

snapshot of the configurations at $t = 100$ (in ZEUS-3D) and iteration 100 (in the Grad–Shafranov code). Note that how the field lines are bent by the transient instabilities in ZEUS-3D but remain smooth in the Grad–Shafranov code. This comparison also illustrates why Grad–Shafranov equilibria are a necessary starting point for ZEUS-3D when aiming to reach stable equilibria for large $M_a \gtrsim 10^{-4}\,M_\odot$. Note that the convergence-matching shown here is not a proof of the stability of the equilibria (Asseo et al. 1978).

5.5 Large perturbations

Next, we investigate what happens when the Grad–Shafranov equilibria are perturbed far from equilibrium, i.e. $\delta B/B \sim 1$; the perturbations considered thus far are small, arising mainly from imperfect translation between the grids of the two codes.

We perturb the magnetic field, while simultaneously respecting the boundary conditions, by setting

$$\boldsymbol{B} \mapsto \boldsymbol{B}\{1 + \delta \sin[\pi(r - R_*)/(r_m - R_*)] \sin\theta\}. \quad (16)$$

Fig. 18(a) shows the fate of this perturbation for different amplitudes δ. Note that the perturbation does not strictly respect flux-freezing because it changes $dM/d\psi$ slightly. None the less, even for significant perturbations, the equilibria are not disrupted – a significant and robust result. For $\delta < 0.2$, μ settles back to within 20 per cent of its initial value. For $\delta > 0.2$, μ does not settle back to its initial value, but it does settle down to some steady value. Again, line-tying plays a key role in conferring such exceptional stability on the system. The evolution also depends on the sign of δ. The perturbation is a low-order spatial mode (in r and θ) and either compresses ($\delta > 0$) or relaxes ($\delta < 0$) the magnetic field, with compression causing a back reaction which increases μ (as can be seen in Fig. 18).

The above perturbation (16) induces an effective redistribution of mass in flux tubes. To avoid this, we perturb the magnetic potential ψ in the Grad–Shafranov code according to

$$\psi \mapsto \psi\{1 + \delta \sin[\pi(r - R_*)/(r_m - R_*)] \sin\theta\} \quad (17)$$

and iterate once to calculate ρ self-consistently without changing $dM/d\psi$, so that the above mass redistribution is performed self-consistently. We then load the self-consistent perturbed equilibrium into ZEUS-3D as before. The results are shown in Fig. 18(b). For a given δ, the amplitude of the oscillations is reduced, confirming that the mass redistribution contributes to the back reaction. The main effect is to bring the final value of μ closer to its initial value for

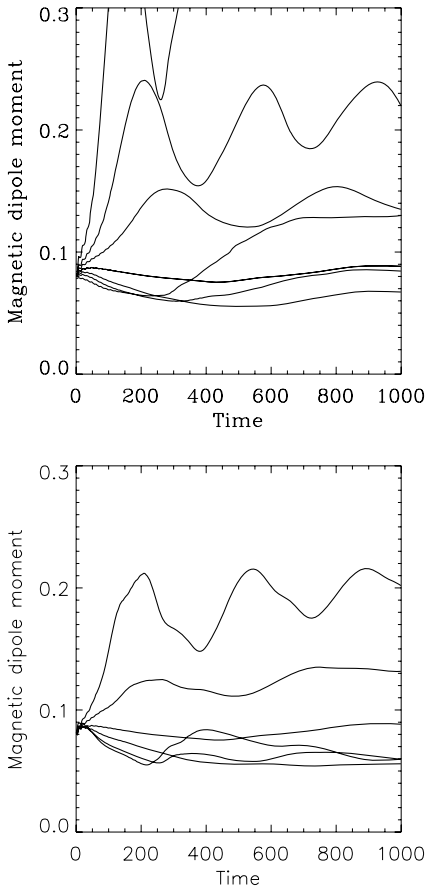

Figure 18. Top panel: magnetic dipole moment as a function of time for perturbation amplitudes $\delta = -1.0, -0.5, -0.25, 0, 0.25, 0.5, 1.0$ (bottom to top), when the magnetic field is perturbed as described in (16) but ρ is not altered. Bottom panel: as above, but with the magnetic field perturbed via (17) and then iterated once through the Grad–Shafranov code to obtain the self-consistent ρ, for $\delta = -0.2, -0.1, 0, 0.1, 0.25, 0.5$ (bottom to top).

$\delta \geqslant 0.5$. The evolution still depends on the sign of δ, suggesting that mass-flux redistribution remains somewhat important.

6 CONCLUSIONS

We find that, when the MHD equilibria computed in PM04 are perturbed, they are marginally stable. The magnetic field remains essentially undisrupted, with the exception of transients that expel a tiny fraction of flux and matter. MHD oscillations, including both acoustic and Alfvén modes, cause μ and ϵ to oscillate about their mean values. Using ZEUS-3D, we extend the results of PM04 to larger M_a in two ways. (i) We add mass through the outer boundary at an artificially accelerated rate which is still slow compared to the MHD equilibration time-scale and oscillation period (as in a real neutron star). We use a bootstrapping method in which the mass is progressively added then allowed to settle to equilibrium. (ii) We increase the density instantaneously uniformly, and then allow the configuration to settle to equilibrium. The equilibria we obtain are stable to Parker modes, as one might expect given that they are the output of a Grad–Shafranov code which follows the full non-linear evolution of Parker instabilities.

The existence of stable magnetic mountains with persistent (albeit oscillating) mass quadrupole moments ($\epsilon \lesssim 10^{-6}$) raises the prospect that accreting millisecond pulsars (Wijnands & van der Klis 1998)

are sources of gravitational radiation. This application is pursued in Melatos & Payne (2005) and Payne & Melatos (2006a). Likewise, the existence of a stable equatorial magnetic belt of intense magnetic field, with its ability to impede thermal transport, has interesting implications for the persistence of millisecond oscillations in the tails of type I thermonuclear X-ray bursts in LMXBs (Muno, Özel & Chakrabarty 2002). This application is pursued in Payne & Melatos (2006b).

6.1 Limitations

The work presented above and in PM04 can be generalized by relaxing certain key assumptions. Some areas to explore include resistive effects (e.g. Ohmic diffusion) (e.g. Konar & Bhattacharya 1997), sinking of accreted material through a 'soft' stellar surface (e.g. Konar & Choudhuri 2004), Hall currents (e.g. Rheinhardt, Konenkov & Geppert 2004), non-axisymmetry and other equations of state. For example, by assuming a hard surface, we end up with densities at the base of the accreted layer that can be unphysically high; it is well known that MHD equilibria can be stable in two dimensions, yet unstable in three dimensions, even with line tying. The magnetization of the accreted plasma also warrants inclusion; it has been ignored by all authors except Uchida & Low (1981).

The main bottleneck hindering progress towards Grad–Shafranov equilibria for $M_\mathrm{a} \gtrsim 10^{-3}\,\mathrm{M}_\odot$ is grid resolution at the magnetic equator. At present, we believe that the only way to alleviate this is by appropriate logarithmic gridding in θ.

Ohmic dissipation due to electron–phonon and electron–impurity scattering (e.g. Bhattacharya & Srinivasan 1999) is not modelled in this paper, to keep the problem manageable. Ultimately, it should be. It is important for magnetic structures $\sim$1 m in size, which develop for $M_\mathrm{a} > 10^{-2}\,\mathrm{M}_\odot$ (Brown & Bildsten 1998; Cumming et al. 2001; Melatos & Payne 2005). Note, however, that non-ideal effects are already present at some level in our calculations accidentally: the grid introduces numerical dissipation, because a field line is defined by linear interpolation between grid points and the error in this interpolation effectively allows matter to move across field lines.

6.2 Instabilities in three dimensions

This paper must be generalized to three dimensions before the stability question is truly settled. As a trivial example, by restricting ourselves to two-dimensional equilibria with $B_\phi = 0$, we suppress unstable modes involving the toroidal magnetic field. The Parker instability in the galactic disc has been studied in three dimensions by Kim et al. (1998), and many simulations of toroidal and non-axisymmetric field structures appear in the plasma physics literature. These can be studied in ZEUS-3D and will be explored in a future paper.

Line-tying boundary conditions, as distinct from periodic boundary conditions, change the character of the basic MHD waves (Goedbloed & Halberstadt 1994). Line-tying boundary conditions generally conflict with the phase relationships between the components of the displacement vector $\boldsymbol{\xi}$ of the three pure modes. MHD waves of a mixed nature occur as a result. Stability is enhanced, because it takes extra energy to bend the longitudinal component of the magnetic field. We do not compare line-tying and periodic boundary conditions quantitatively here but point out that line-tying enhances stability even in three dimensions (Goedbloed & Halberstadt 1994).

Short-wavelength ballooning instabilities are stabilized by line-tying until the overpressure at the top of the stellar crust exceeds the magnetic pressure by a factor of $8R_* \arcsin(b^{-1/2})/h_0$ (Litwin et al. 2001). While they are predicted to occur within h_0 of the surface, we do not observe them in these simulations. Resistive ballooning (Velli & Hood 1986) and resistive Rayleigh–Taylor modes (Khan & Bhatia 1993) are not considered by virtue of our restriction to ideal-MHD, but they are known to be common in distorted axisymmetric equilibria similar to those in Fig. 1(a). These instabilities can allow plasma slippage faster than Ohmic diffusion, but slower than the Alfvén time.[2] To properly model these instabilities globally, large toroidal quantum numbers need to be considered (Huang, Zweibel & Sovinec 2006).

ACKNOWLEDGMENTS

This research was supported in part by an Australian postgraduate award and a David Hay write-up award.

REFERENCES

Arons J., Burnard D. J., Klein R. I., McKee C. F., Pudritz R. E., Lea S. M., 1984, in Woosley S. E., ed., High Energy Transients in Astrophysics. Am. Inst. Phy., New York, p. 215
Asseo E., Cesarsky C. J., Lachieze-Rey M., Pellat R., 1978, ApJ, 225, L21
Bhattacharya D., Srinivasan G., 1999, in Lewin W. H. G., van Paradijs J., van den Heuvel E. P. J., eds, X-ray Binaries. Cambridge Univ. Press, Cambridge, p. 235
Bisnovatyi-Kogan G. S., Komberg B. V., 1974, Sov. Astron., 18, 217
Brown E. F., Bildsten L., 1998, ApJ, 496, 915
Burderi L., Possenti A., Colpi M., di Salvo T., D'Amico N., 1999, ApJ, 519, 285
Cumming A., Zweibel E., Bildsten L., 2001, ApJ, 557, 958
Cumming A., Arras P., Zweibel E., 2004, ApJ, 609, 999
Goedbloed J. P., Halberstadt G., 1994, A&A, 286, 275
Goedbloed J. P. H., Poedts S., 2004, Principles of Magnetohydrodynamics. Cambridge Univ. Press, Cambridge
Hameury J. M., Bonazzola S., Heyvaerts J., Lasota J. P., 1983, A&A, 128, 369
Huang Y.-M., Zweibel E. G., Sovinec C. R., 2006, Phys. Plasmas, 13, 2102
Khan A., Bhatia P. K., 1993, Phys. Scr., 48, 607
Kim J., Hong S. S., Ryu D., Jones T. W., 1998, ApJ, 506, L139
Klimchuk J. A., Sturrock P. A., 1989, ApJ, 345, 1034
Konar S., Bhattacharya D., 1997, MNRAS, 284, 311
Konar S., Choudhuri A. R., 2004, MNRAS, 348, 661
Litwin C., Brown E. F., Rosner R., 2001, ApJ, 553, 788
Melatos A., Payne D. J. B., 2005, ApJ, 623, 1044
Melatos A., Phinney E. S., 2001, Publ. Astron. Soc. Aust., 18, 421
Mouschovias T., 1974, ApJ, 192, 37
Mouschovias T., 1996, in Tsinganos K. C., ed., NATO ASI Ser. C, Vol. 481, Solar and Astrophysical Magnetohydrodynamic Flows. Kluwer, Dordrecht, p. 475
Muno M. P., Özel F., Chakrabarty D., 2002, ApJ, 581, 550
Muslimov A. G., Tsygan A. I., 1985, Sov. Astron. Lett., 11, 80
Parker E., 1966, ApJ, 145, 811
Payne D. J. B., Melatos A., 2004, MNRAS, 351, 569 (PM04)
Payne D. J. B., Melatos A., 2006a, ApJ, 641, 471
Payne D. J. B., Melatos A., 2006b, ApJ, 652, 597
Rheinhardt M., Konenkov D., Geppert U., 2004, A&A, 420, 631
Romani R. W., 1990, Nat, 347, 741
Shibazaki N., Murakami T., Shaham J., Nomoto K., 1989, Nat, 342, 656
Srinivasan G., Bhattacharya D., Muslimov A., Tsygan A., 1990, Curr. Sci., 59, 31
Stone J. M., Norman M. L., 1992a, ApJS, 80, 753
Stone J. M., Norman M. L., 1992b, ApJS, 80, 791

[2] J. Arons, private communication.

Strohmayer T. E., Bildsten L., 2006, in Lewin W. H. G., van der Klis M., eds, Compact Stellar X-Ray Sources. Cambridge Univ. Press, Cambridge, p. 113
Taam R. E., van den Heuvel E. P. J., 1986, ApJ, 305, 235
Tauris T. M., van den Heuvel E. P. J., Savonije G. J., 2000, ApJ, 530, L93
Uchida Y., Low B. C., 1981, JA&A, 2, 405
Urpin V., Geppert U., 1995, MNRAS, 275, 1117
Urpin V., Konenkov D., 1997, MNRAS, 284, 741
van den Heuvel E. P. J., Bitzaraki O., 1995, A&A, 297, L41
Velli M., Hood A. W., 1986, Sol. Phys., 106, 353
Wijers R. A. M. J., 1997, MNRAS, 287, 607
Wijnands R., van der Klis M., 1998, Nat, 394, 344

APPENDIX A: MAGNETIC BURIAL IN ZEUS-3D

In this appendix, we explain briefly how to simulate the problem of magnetic burial in ZEUS-3D, so that the reader can reproduce and generalize our results.[3] For details on the general design and operation of ZEUS-3D, please consult Stone & Norman (1992a,b).

After discussing the control variables in ZEUS-3D, we provide several test cases for reference. The Parker instability in rectangular coordinates, whose non-linear evolution was computed by Mouschovias (1974, 1996), tests the basic functionality of ZEUS-3D. An unmagnetized, isothermal atmosphere in spherical coordinates tests the boundary conditions on ρ and $\boldsymbol{v}$. A magnetized, isothermal atmosphere in spherical coordinates tests the boundary conditions on $\boldsymbol{B}$ and yields the equilibrium state for $M_{\rm a} = 0$.

A1 Control variables

The number of active grid zones in each coordinate, ggen1:nbl and ggen2:nbl for i and j, respectively, is $G_x \times G_y$ (typically 128×128). In addition, there are two ghost zones at each edge of the grid, for setting boundary conditions. The zones in, say, the i direction (r in spherical coordinates) can scale geometrically using ggen1:x1rat, such that the width of zone (i+1) is x1rat times zone i. This is how we implement logarithmic coordinates to increase grid resolution near the stellar surface, and to match input data from the Grad–Shafranov code in PM04 (Section A7). There are several conditional compilation switches which control the geometry. To implement two dimensions, enable KSYM, and set the number of zones in the third ordinate, ggen3:nbl to 1. For Cartesian coordinates, enable XYZ; for spherical polar coordinates, enable RTP. When printing out the grids, we use nxpx = nypx = 400 pixel and suppress the third dimension (z or ϕ) by setting pixcon:ipixdir = 3.

The results in this paper assume an isothermal equation of state for simplicity, thus ISO is enabled. Self-gravity, GRAV, is disabled. Dimensionless quantities are chosen as follows: $\tilde{\mu}_0 = 1$ (automatic in ZEUS-3D), $\tilde{G} = 1$ (set grvcon:g=1), $\tilde{c}_{\rm s} = 1$ (set eqos:ciso=1) and $\tilde{h}_0 = 1 (h_0 = c_{\rm s}^2 R_*^2/GM_*)$. With these choices, the basic units of mass, magnetic field and time become $M_0 = h_0 c_{\rm s}^2/G$, $B_0 = [\mu_0 c_{\rm s}^4/(G h_0^2)]^{1/2}$ and $\tau_0 = h_0/c_{\rm s}$. In ideal-MHD, the evolution is controlled by the geometry as well as the ratio of magnetic to thermal pressure, $\alpha = B^2/(\mu_0\, c_{\rm s}^2\, \rho)$; the physical units of B and ρ do not enter separately. Varying $\tilde{G}$, set to one by default, changes the unit conversions but not the physics. ZEUS-3D may be run as a hydrodynamic code without magnetic fields by disabling MHD, reducing the run time.

The time-step $\Delta t_{\rm Z}$ is adjusted adaptively so that the Courant–Friedrichs–Lewy stability condition is satisfied in every zone, with the tolerance determined by the Courant number (hycon:courno = 0.5 by default). In the case of an isothermal atmosphere and subsonic fluid motions, it is set by max ($c_{\rm s}$, $v_{\rm A}$). Since one has $v_{\rm A} \propto 1/\rho \propto {\rm e}^{\bar{x}}$

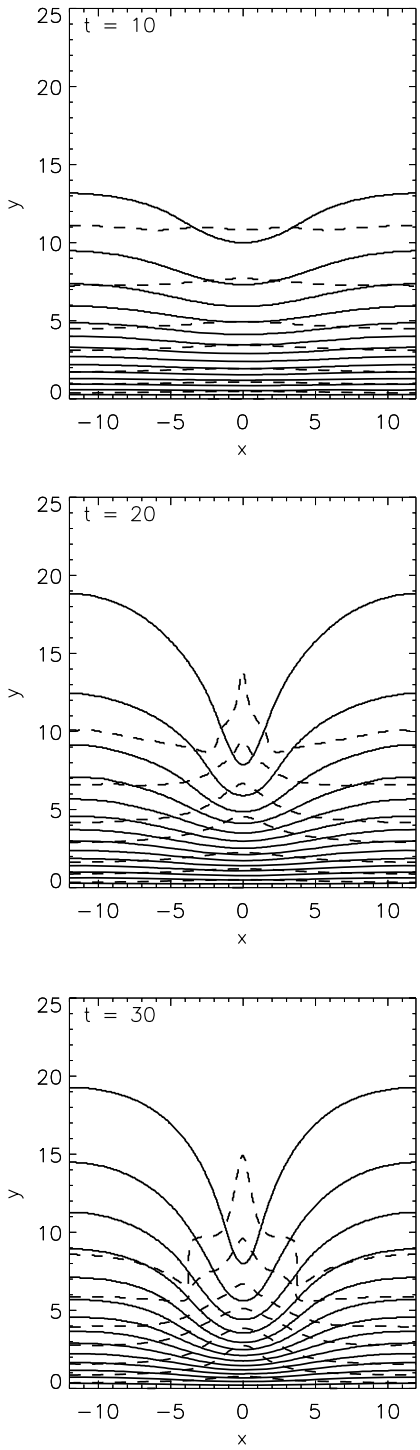

Figure A1. Non-linear evolution of the Parker instability, showing magnetic flux surfaces (solid) and isodensity contours (dashed) for $(X, Y) = (12, 25)$, $\tilde{\tau} = 10,\ 20,\ 30$ and $G_x = G_y = 64$

[3] This work also serves as a prototype of a simulation pipeline being developed by the Australian Virtual Observatory. We have demonstrated a preliminary version of this pipeline in which hydromagnetic equilibria generated by the time-independent, Grad–Shafranov code described in PM04 are output in a standard format (VOTable) and fed into ZEUS-3D to be evolved in time.

Table A1. Gravitational, magnetic and kinetic energies (dimensionless units) resulting from a point mass located at $R_{\rm eff}$ such that $\tilde{M}/\tilde{R}_{\rm eff}^2 = 1$. The initial state is the equilibrium given by (A1) and (A2), with $\tilde{\tau} = 10$ and $(X, Y) = (7, 25)$, perturbed as described in the text.

$\tilde{R}_{\rm eff}$	$\tilde{W}_{\rm g}$	$\tilde{W}_B$	$\tilde{W}_{\rm k}$
7.6×10^2	-1.03×10^3	12.9	1.03×10^{-1}
7.6×10^2	-1.06×10^4	14.0	1.75×10^{-3}
7.6×10^3	-1.06×10^5	14.0	1.32×10^{-5}
7.6×10^4	-1.06×10^6	14.0	1.22×10^{-6}
7.6×10^5	-1.06×10^7	14.0	1.69×10^{-6}
7.6×10^6	-1.06×10^8	14.0	1.75×10^{-6}

in a typical isothermal atmosphere, the code is limited in the range of altitudes and densities that it can faithfully simulate. The grid is dumped at times separated by pixcon:dtpix and the code runs for a maximum time pcon:tlim.

A2 Verifying the Parker instability in a rectangular geometry

A test case which is easy to implement (and relevant to the problem of magnetic burial) is the Parker or magnetic Rayleigh–Taylor instability (Parker 1966; Mouschovias 1974, 1996). The initial equilibrium state is a semi-infinite, exponentially stratified atmosphere in a uniform gravitational field, with a magnetic field perpendicular to the gravitational force. This configuration is unstable to overturn (slow MHD) modes longer than a critical wavelength $\lambda_{\rm crit}$.

We simulate the Parker instability in the region $-X \leqslant \tilde{x} \leqslant X, 0 \leqslant \tilde{y} \leqslant Y$. A uniform gravitational acceleration g_y in the y direction is implemented in ZEUS-3D by placing a point mass far from the simulation box, at $\tilde{y} = \tilde{R}_{\rm eff} \gg Y$. The boundary conditions are set to be periodic at $\tilde{x} = \pm X$ (niib, noib = 4) and reflecting at $\tilde{y} = 0, Y$ (nijb = nojb = 1).

In dimensionless units, the equilibrium initial conditions are

$$\tilde{\rho}(\tilde{x}, \tilde{y}) = 0.5 \exp[-\tilde{y}/(1+\alpha)] \tag{A1}$$

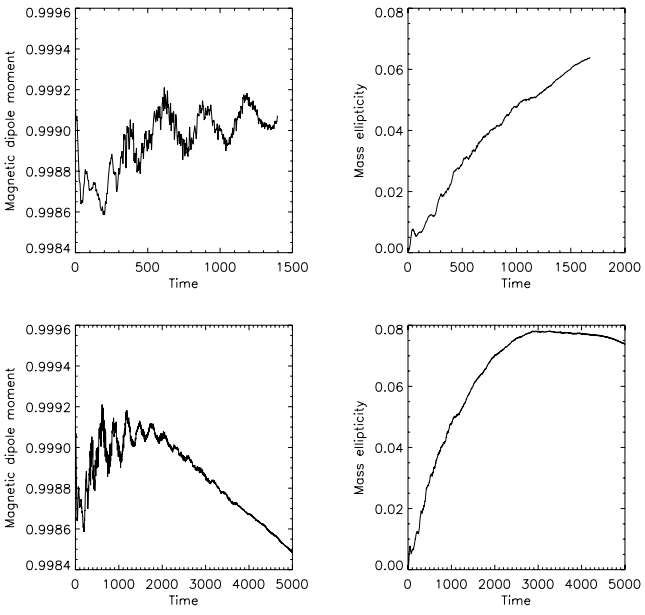

Figure A2. The dipole (left) and mass ellipticity (right) as a function of time for an isothermal atmosphere with $a = 100$ and $\tilde{r}_{\rm m} = 110$ in a 64×64 grid. Parameters: $\rho_0 = 1$ and $B_0 = 0.1$, x1rat = 1.03.

Table A2. Proportion of the initial mass lost from the simulation volume, and run time for $\tilde{t} = 100$, as functions of the dimensionless hydrostatic scaleheight a^{-1}. The grid size used was 50×100. Naturally, the relative run times are more useful than the absolute.

a	$\tilde{r}_{\rm m}$	Per cent mass loss	Run time (min)
50	60	0.5	5
50	55	14.1	5
50	52	17.0	5
20	30	1.72	3
40	50	1.2	4
100	110	0.3	10
500	510	0.1	20

and

$$\tilde{A}_z(\tilde{x}, \tilde{y}) = 2(1+\alpha) \exp[-\tilde{y}/2(1+\alpha)], \tag{A2}$$

with $\tilde{B}_x = (\nabla \times \tilde{A})_x = -{\rm e}^{-\tilde{y}/2(1+\alpha)}$. The initial velocity perturbation is taken as $\tilde{v}_y = \epsilon \sin(\pi\tilde{y}/Y)\cos(\pi\tilde{x}/X)$, where, for $\epsilon = 0.3$, the kinetic energy equals 0.23 per cent of the magnetic energy; cf. Mouschovias (1996).

The stability condition is tested by importing a stable equilibrium state, with $X < \lambda_{\rm crit}/2$, and checking that the kinetic energy remains negligible compared to the magnetic and gravitational potential energies. The ratio of the kinetic energy to the total energy is given in Table A1, scaling as $\tilde{R}_{\rm eff}^{-2}$ for $\tilde{R}_{\rm eff} \lesssim 10^5$. We choose $\tilde{R}_{\rm eff} = 7.6 \times 10^4$ for most runs. This test also confirms that the equilibrium is stable for $(X, Y) = (7, 25)$, just below the critical value $\lambda_{\rm crit}/2 = 7.26$ (Mouschovias 1974), and is unstable for $(X, Y) = (8, 25)$.

We also set $(X, Y) = (12, 25)$ and verify the output against the results given in fig. 3 of Mouschovias (1996). We choose the same units, namely $c_{\rm s} = 6.2$ km s^{-1}, $h_0 = 1.3 \times 10^{18}$ m, $\tau_0 = r_0/c_{\rm s} = 6.5 \times 10^6$ yr, $M_0 = 5.8 \times 10^{17}$ kg, $\rho_0 = 2.9 \times 10^{-37}$ kg m^{-3}, $B_0 = 3.7 \times 10^{-18}$ T. (To have exactly the same units as Mouschovias 1996 chooses $\tilde{G} = 6.67 \times 10^{-17}$ in ZEUS-3D.) Fig. A1 shows the ZEUS-3D results at the three times displayed in fig. 3 of Mouschovias (1996). The results are in good accord, differing by less than 5 per cent. A mountain is clearly present where the magnetic field bends down in the negative y direction.

A3 Spherical, isothermal atmosphere, zero magnetic field

Having verified a known solution, we now move closer to our goal and consider spherical geometry (RTP). We consider first an isothermal atmosphere with no magnetic field to test the effect of the boundary conditions. In spherical geometry, the curvature of the star, characterized by $a = R_*/h_0 \sim 2 \times 10^4$, enters the problem. To cope with this large value, we scale coordinates in ZEUS-3D logarithmically (Section A1). However, the code halts prematurely when the time-step Δt_Z becomes too small; for $a > 10^3$, it does not run at all. The problem is most severe far from the surface, where ρ is small, $v_{\rm A}$ is large, and Δt_Z is small. As an initial test case in spherical coordinates, we set up a spherical isothermal atmosphere with a negligible magnetic field ($\alpha = 4 \times 10^{-8}$) in 2D (single quadrant). The initial condition is an exponential isothermal atmosphere

$$\tilde{\rho}(\tilde{r}, \theta) = \exp[-a(\tilde{r} - a)/\tilde{r}] \approx \exp(-\tilde{x}) \tag{A3}$$

threaded by a dipolar magnetic vector potential

$$\tilde{A}_\phi(\tilde{r}, \theta) = 10^{-10}\tilde{r}^{-2} \sin\theta. \tag{A4}$$

The boundary conditions are reflecting at the pole ($B_\theta = 0$, nijb = 1) and at the equator ($B_r = 0$, nijb = 5), dipolar at the surface

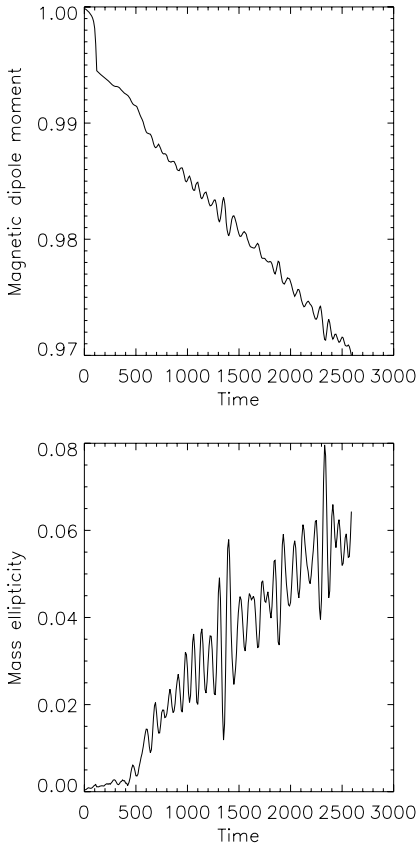

Figure A3. The dipole (left) and mass ellipticity (right) as a function of time for an isothermal atmosphere with $a = 500$ and $\tilde{r}_{\rm m} = 510$ in a 64×64 grid. Parameters: $\rho_0 = 1$ and $B_0 = 0.1$, x1rat = 1.03.

Table A3. Errors as a function of grid size as measured by the deviation of μ and ϵ from theoretical values for $\mu_{\rm t}$ and $\epsilon_{\rm t} = 0$ for $a = 100$, $\tilde{r}_{\rm m} = 110$ and $\tilde{t} = 0$.

Grid size	$\mu/\mu_{\rm t}$	ϵ
64×64	0.999 101	$4.322\,68 \times 10^{-4}$
50×100	1.003 032	$2.637\,89 \times 10^{-4}$
150×150	1.001 214	$4.523\,17 \times 10^{-4}$
300×300	1.000 302	$1.265\,03 \times 10^{-4}$

(niib = 3, i.e. inward flow at zero velocity, fixed density, dipolar magnetic field) and free at the outer boundary ($\tilde{r} = \tilde{r}_{\rm m}$) (niob = 2, outward flow). Note that, in ZEUS-3D, a fixed magnetic field must be accompanied by inflow, even if the inflow is at zero speed.

The experiment described in this section aims to calibrate the role of the outer boundary condition. Equations (A3) and (A4) almost describe a force-free equilibrium except that matter can evaporate through the outer boundary. However, alternative boundary conditions offered in ZEUS-3D are not appropriate, e.g. inflow artificially pins the magnetic field lines at the boundary. The amount of mass loss is monitored and $\tilde{r}_{\rm m}$ is chosen large to minimize it. There is a trade off between minimizing mass loss as well as simulation run time (determined primarily by Δt_Z), as illustrated in Table A2. Logarithmic grid scaling has little effect on the amount of mass which evaporates through the outer boundary. The outer boundary condition artificially increases the dipole moment at large r, as discussed in the main text and illustrated in Fig. 3(f). The run time is reduced if the magnetic calculations are switched off by disabling MHD; the results are indistinguishable. The results in Table A2 are for $R_* = 6.4 \times 10^6$ m, $M_* = 6.0 \times 10^{24}$ kg, $c_{\rm s} = 290\,{\rm m\,s^{-1}}$, $h_0 = 8.4 \times 10^3$ m. With these choices, the basic units become $M_0 = c_{\rm s}^2/G = 1.2 \times 10^{15}$ kg, $\rho_0 = M_0/r_0^3 = 2.1 \times 10^3\,{\rm kg\,m^{-3}}$, $B_0 = [\mu_0\, c_{\rm s}^4/(Gr_0^3)]^{1/2} = 15$ T, $\tau_0 = r_0/c_{\rm s} = 29$ s; the alert reader will note that these parameters describe the Earth!

A4 Spherical, isothermal atmosphere, dipole magnetic field

As a prelude to testing the stability of the Grad–Shafranov equilibria found by PM04, we consider the simpler situation of the spherical, isothermal atmosphere (Section A3) threaded by a substantial dipolar magnetic field. Note that this is a valid force-free equilibrium state [$(\nabla \times \boldsymbol{B}) \times \boldsymbol{B} = 0$ in (1) except at $r = 0$], except for evaporation. This configuration corresponds to the pre-accretion neutron star with $M_{\rm a} = 0$. It serves to calibrate ZEUS-3D and estimate the magnitude of numerical errors.

The relevant neutron star parameters are $R_* = 10^4$ m, $M_* = 1.4\,{\rm M}_\odot$, $c_{\rm s} = 10^6\,{\rm m\,s^{-1}}$. With these choices, the basic units become $M_0 = c_{\rm s}^2/G = 1.5 \times 10^{22}$ kg, $\rho_0 = M_0/r_0^3 = 9.5 \times 10^{22}\,{\rm kg\,m^{-3}}$, $B_0 = [\mu_0\, c_{\rm s}^4/(Gr_0^3)]^{1/2} = 3.5 \times 10^{14}$ T, $\tau_0 = r_0/c_{\rm s} = 5.4 \times 10^{-7}$ s. However, as discussed in Section 3.3, we consider a scaled version of the real star with $a = 50$, leaving the physical scaleheight, $h_0 = c_{\rm s}^2\, R_*^2/(GM_*) = 0.54$ m, unchanged.

To estimate the errors in the code, we calculate the magnetic dipole moment and mass quadrupole moment and compare to the theoretical values $\mu = 0.5a^3\,\tilde{B}_*$ and $\epsilon = 0$ in Table A3. For $b = 1$, we obtain $\epsilon = 1.026\,19$; for $b = 3$, $\epsilon = 1.233\,73$. The errors are less than

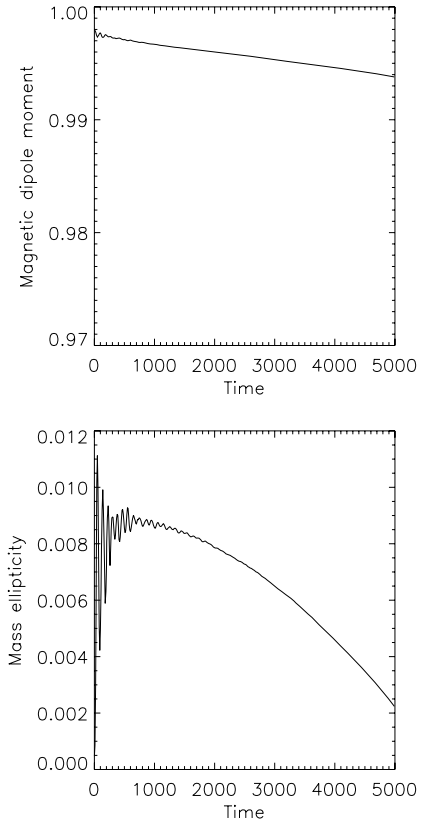

Figure A4. The dipole (left) and mass ellipticity (right) as a function of time for an isothermal atmosphere with $a = 40$ and $\tilde{r}_{\rm m} = 50$ in a 64×64 grid. Parameters: $\rho_0 = 1$ and $B_0 = 0.1$, x1rat = 1.03.

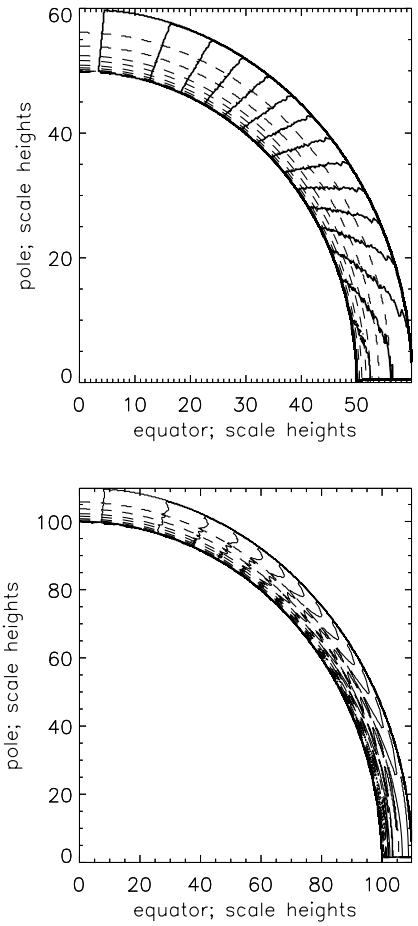

Figure A5. Isothermal atmosphere with dipolar magnetic field. The kinks in the magnetic field lines (solid) are due to numerical dissipation. Parameters: $a = 50$, $\tilde{r}_\mathrm{m} = 60$, $\tilde{\tau} = 66$, 150×150 grid (left); $a = 100$, $\tilde{r}_\mathrm{m} = 110$, $\tilde{\tau} = 66$, 50×100 grid x1rat = 1.1 (right).

Table A4. The time taken for numerical dissipation to halt the simulation for $a = 100\,\tilde{r}_\mathrm{m} = 110$, and a 50×100 grid, as a function of ggen1:x1rat, the geometric ratio in the rescaled coordinate r.

x1rat	Δt_A	Δt_s	Time to halt (τ_0)
1	$2.937\,14 \times 10^{-3}$	0.20	10.26
1.02	$4.641\,49 \times 10^{-3}$	0.31	17.28
1.03	$5.778\,38 \times 10^{-3}$	0.38	27.22
1.05	$8.124\,72 \times 10^{-3}$	0.52	55.62
1.10	$9.679\,61 \times 10^{-3}$	0.01	66.71
1.102	$9.634\,28 \times 10^{-3}$	0.01	43.48

1 per cent. Fig. A2 shows how the dipole and mass ellipticity vary with time for these cases. The dipole moment is accurate to <0.2 per cent. The minor variations are caused by numerical jitter (also see Fig. A5) and evaporation at the outer boundary (Section 5.4. The dependence of the error on grid size is tabulated in Table A3.

A5 Outer boundary

The outflow condition at the outer boundary has minimal effect on the evolution if the outer boundary is sufficiently far away. To test this, we try several values of $\tilde{r}_\mathrm{m}$, keeping $\tilde{r}_\mathrm{m}$ small enough so that the Alfvén time-step, set by the Courant condition with $v_\mathrm{A} \propto B^2/\rho$, is not too short.

Numerical dissipation occurs in ZEUS-3D for runs longer than $\gtrsim 10^5$ time-steps. Kinks in the magnetic field appear at grid points, as illustrated in Fig. A5. If the outer boundary is set too many scale-heights away, the minimum density across the grid is very low, the maximum Alfvén velocity is very high, and the time-step, Δt_Z, determined by the Courant condition, is very short. This means that (i) the simulation takes a very long time to run, and (ii) the numerical dissipation causes the simulation to stop. For $a = 50$ and $\tilde{r}_\mathrm{m} = 70$, the code stops at $\tilde{\tau} < 2$; for $\tilde{r}_\mathrm{m} = 80$, it stops at $\tilde{\tau} < 0.2$. For $a = 100$ and $\tilde{r}_\mathrm{m} = 110$, the code stops at $\tilde{\tau} = 10.26$, but with ggen1:x1rat = 1.03 instead of 1, it continues until $\tilde{\tau} = 27.22$. For $a = 1000$ and $\tilde{r}_\mathrm{m} = 1010$, the code stops immediately. Throughout the paper, we use $\tilde{r}_\mathrm{m} = 60$, so that the runs are long enough to give sufficient time to assess the stability of the equilibria. Table A4 shows how the grid ratio affects the time to halt.

A6 Converting to realistic a values and between codes

Here we give the formulae for converting between the Grad–Shafranov code and ZEUS-3D. Furthermore, we detail the effects of converting from a small ($a = 50$) to a realistic ($a \approx 10^4$) star. With h_0 fixed, but allowing a to vary, we have $R_* = ah_0 = 27(a/50)$ m, $M_*/\mathrm{M}_\odot = a^2 h_0 c_\mathrm{s}^2/(G\,\mathrm{M}_\odot) = 1.0138 \times 10^{-5}(a/50)^2$, and

$$\frac{M_\mathrm{c}}{\mathrm{M}_\odot} = 6.1 \times 10^{-15} \left(\frac{a}{50}\right)^4 \left(\frac{B_*}{10^8\mathrm{T}}\right)^2 \left(\frac{c_\mathrm{s}}{10^6\,\mathrm{m\,s^{-1}}}\right)^{-4}. \quad \text{(A5)}$$

h_0 is the dimensionless unit of length. The dimensionless units in the Grad–Shafranov code (subscript 'G') are $\rho_\mathrm{0,G} = M_\mathrm{a}/h_0^3 = 9.8 \times 10^{-16}\ (m/0.16)(a/50)^4\ \mathrm{kg\,m^{-3}}$, $B_\mathrm{0,G} = B_* a^2/(2b) = 4.2 \times 10^{10}\ (a/50)^2(b/3)^{-1}$ T. In ZEUS-3D (subscript 'Z'), $\rho_\mathrm{0,Z} = c_\mathrm{s}^2/(Gh_0^3) = 9.6 \times 10^{22}\ \mathrm{kg\,m^{-3}}$, $B_\mathrm{0,Z} = (\mu_0/Gh_0^3)^{1/2} c_\mathrm{s}^2 = 3.5 \times 10^{14}$ T. For conversion from the equilibrium code to ZEUS-3D, the factors are $\rho_\mathrm{G,Z} = \rho_\mathrm{0,G}/\rho_\mathrm{0,Z} = GM_\mathrm{a}/c_\mathrm{s}^2 = 1.3 \times 10^{-7}\ (m/0.16)(a/50)^4$ and $B_\mathrm{G,Z} = B_\mathrm{0,G}/B_\mathrm{0,Z} = B_* a^2/(2bc_\mathrm{s}^2)(Gh_0^3/\mu_0)^{1/2} = 1.2 \times 10^{-4}(a/50)^2\,(b/3)^{-1}$.

A7 Logarithmic coordinates

PM04 concentrated maximum grid resolution near the equator and stellar surface where $\nabla\rho$ and $\nabla\psi$ are greatest, by employing logarithmic stretching:

$$\tilde{x_1} = \log(\tilde{x} + \mathrm{e}^{-L_x}) + L_x, \quad \text{(A6)}$$

$$\tilde{y_1} = -\log[1 - (1 - \mathrm{e}^{-L_y})\tilde{y}]. \quad \text{(A7)}$$

To implement these coordinates in ZEUS-3D, set ggen1:x1rat to $(X\mathrm{e}^{L_x} + 1)^{(G_x - 1)^{-1}}$, where $0 \leqslant \tilde{x} \leqslant X$ and L_x controls the 'zoom'. Radial logarithmic scaling gives less grid resolution near the outer boundary where the density is least and thus Δt_Z is greater and ZEUS-3D runs for a longer time.

When importing a Grad–Shafranov equilibrium (PM04), whose grid is linear in $y = \cos\theta$, into ZEUS-3D, whose grid is (in many cases) logarithmic in y, there is no trivial multiplicative factor relating $\tilde{y}_1$ and the required logarithmic θ scaling through ggen1:x2rat. The problem can be overcome by rewriting the Grad–Shafranov code such that its grid is logarithmic in θ. This problem is an obstacle in certain sorts of numerical experiments, e.g. the bootstrapping method in Section 4.2.

This paper has been typeset from a TEX/LATEX file prepared by the author.